Navigation Algorithms and Observability Analysis for Formation Flying Missions

Paul J. Huxel* and Robert H. Bishop†
University of Texas at Austin, Austin, Texas 78712

DOI: 10.2514/1.41288

Navigation algorithms and the corresponding observability analysis for formation flying missions are developed. In particular, the advantages and concerns associated with the use of combinations of inertial and relative measurements are examined. The methodology of the observability analysis relates the physical geometry of the observers, as well as the spacecraft formation, to a measure of linear time-invariant system observability. The investigation also examines the robustness of the extended Kalman filter while simultaneously processing inertial and relative range measurements. It has been shown that processing relative range measurements in conjunction with inertial range measurements can directly increase the accuracy of the inertial state estimate. However, it has also been shown that when there is relatively large uncertainty in the state estimate, the addition of relative measurements can cause an otherwise convergent filter to diverge. This paper considers several methods for preventing this divergence, as well as an in-depth examination of second-order terms to explain the basis of the problem. In particular, to illustrate their potential significance, analytical bounds are derived for the second-order terms.

I. Introduction

AS SPACE exploration and space technologies advance, so do the ambition and complexity of space missions. In particular, the interest in formation flying missions is on the rise. Using innovative formations of multiple spacecraft, these missions can accomplish what would be extremely difficult and often too costly using only one spacecraft. With missions ranging from small formations for remote sensing and mapping to elaborate formations acting as interferometers and telescopes, precise and accurate inertial navigation will be vital for success. Although the increase in spacecraft creates a more complex mission, it also provides a measurement-rich environment. For example, employing relative range measurements (between each spacecraft), a formation of p spacecraft can provide $p(p - 1)/2$ unique relative measurements. Moreover, the use of these relative range measurements can directly contribute to improved navigation accuracy of the inertial state estimate. This increase in navigation accuracy comes at the cost of a decrease in robustness. Robustness, in this context, is defined to be the ability of the navigation filter to converge for a wide range of state error covariances. This paper provides a framework to analyze navigation performance for formation flying missions and also presents methods to enhance robustness. For additional information, including a review of existing literature on these topics, the reader is referred to Huxel [1].

II. Mission Description and Models

The mission under consideration consists of two flight segments: a cislunar (i.e., Earth–moon) transfer trajectory and a circular polar lunar orbit. During the cislunar transfer trajectory, a single cluster of spacecraft is examined in two dimensions. Figure 1 shows the cislunar transfer trajectory, the trajectory of the moon, and the Earth

at the origin. The dotted lines denote parts of the complete trajectories not traversed during the transfer. The triangles and diamond denote the "snapshot" locations of the five Earth–moon libration points when the moon crosses the X_I axis after transfer time t_{trans}.

The significance of the libration points is the placement of tracking stations at L_4 and L_5 during the cislunar transfer segment and additionally at L_2 during the lunar orbit segment. During the cislunar transfer segment, these tracking stations provide range measurements that have cyclical trends with distances (from the stations to the cluster) ranging from a minimum of about 1.89×10^5 km to a maximum of about 4.85×10^5 km. The ranges from the libration point tracking stations for the lunar orbit segment also have cyclical trends. Ranges from the station at L_2 are approximately 0.645×10^5 km, whereas those from the stations at L_4 and L_5 have a minimum of about 3.83×10^5 km and a maximum of about 3.86×10^5 km; a difference roughly equal to twice the orbital semimajor axis (i.e., the extremum occur at the nodal crossings on each side of the orbit).

Upon reaching the moon, the cluster separates and multiple spacecraft in formation about a reference point in a 100-km-altitude circular polar orbit are examined. As illustrated in Fig. 2, the polar orbit is oriented such that the line of nodes is parallel to the Y_I axis, which results in the orbit plane being coplanar with the Y_I-Z_I plane. As shown in Fig. 1, at the start of this mission segment, the orientation of the Earth is such that the Earth–moon line is initially aligned with the X_I axis and then slowly rotates (13.2 deg/day) in the X_I-Y_I plane counterclockwise about the Z_I axis.

The navigation and observability analysis of the lunar orbit mission segment examines two formation variations: a one-plane, two-spacecraft formation and a three-plane, six-spacecraft formation. In both formations, each plane consists of two spacecraft traveling in a 100-km-altitude circular orbit with the line of nodes of each plane along the Y_I axis. The first formation plane employs the reference point orbit. The second formation builds on the first by adding two secondary planes, each tilted a distance defined as $b = 10$ km in opposite directions away from the first plane. Within each of the three planes, two spacecraft slots are staggered about the projected argument of latitude of the reference point such that the range between coplanar spacecraft is also chosen to be $b = 10$ km. In terms of orbital elements, the distance b corresponds to an inclination difference (and angular spacing between coplanar spacecraft) of about 0.3 deg. Figure 2 illustrates an exaggerated formation ($b = 500$ km) for visualization purposes.

The crosslink (spacecraft-to-spacecraft) range measurement profile is periodic with the orbit. In particular, the ranges between

---

*Research Assistant, Aerospace Engineering and Engineering Mechanics, 210 East 24th Street, 1 University Station; currently Charles Stark Draper Laboratory, Inc., Cambridge, Massachusetts 02139.

†Professor, Aerospace Engineering and Engineering Mechanics, 210 East 24th Street, 1 University Station. AIAA Fellow.
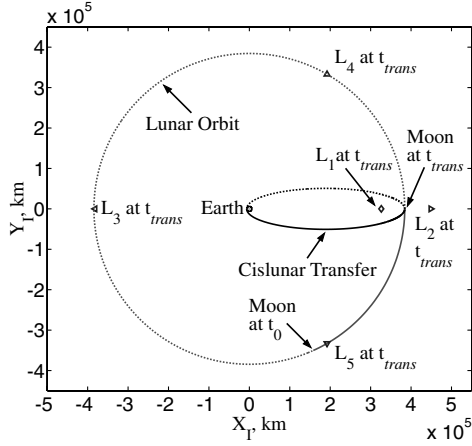
Fig. 1 Cislunar transfer trajectory and libration point geometry (at time t_{trans}).
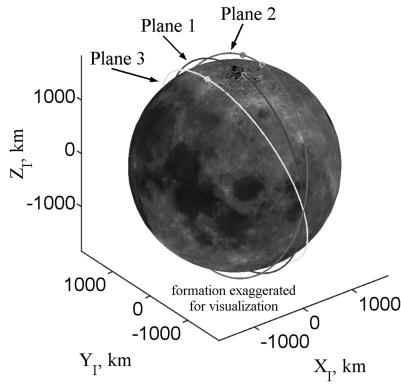

Fig. 2 Exaggerated lunar formation orbit planes.

spacecraft oscillate in an interval with a minimum of about 3 km and a maximum of about 26 km, while coplanar spacecraft maintain a distance of 10 km. This large difference in magnitude between tracking station range measurements and crosslink range measurements will be of particular interest in light of the discussion presented in Sec. V.

In general, the state to be estimated consists of the body-centered inertial position $\mathbf{r}$ and velocity $\mathbf{v}$ vectors for p spacecraft, such that

$$\mathbf{x} = [\, \mathbf{r}_1^T \quad \cdots \quad \mathbf{r}_p^T | \mathbf{v}_1^T \quad \cdots \quad \mathbf{v}_p^T \,]^T \qquad (1)$$

To make the observability and fusion analyses manageable and lucid, extraneous error sources and potential numerical instabilities have been avoided whenever possible. For this reason, simple Keplerian motion without perturbations is used for both the true environment and the filter dynamic models, such that

$$\dot{\mathbf{x}} = \mathbf{f}(\mathbf{x}) = [\, f_1 \quad \cdots \quad f_n \,]^T = [\, \mathbf{v}_1^T \quad \cdots \quad \mathbf{v}_p^T | \mathbf{g}_1^T \quad \cdots \quad \mathbf{g}_p^T \,] \quad (2)$$

where

$$\mathbf{g}_j = \ddot{\mathbf{r}}_j = -\frac{\mu}{\|\mathbf{r}_j\|^3}\mathbf{r}_j \qquad (3)$$

for $j = 1, \ldots, p$, and μ is the gravitational constant of the central body. Moreover, unless otherwise stated, system noise is not implemented (i.e., $\mathbf{Q}_{\text{spec}} = \mathbf{0}$, see Sec. III).

Another reason for choosing the Keplerian dynamic model was to simplify the derivation and computation of the Jacobian and Hessian matrices that will later be required by the Kalman filter. Using Eqs. (1) and (2), the Jacobian matrix can be partitioned as

$$\frac{\partial \mathbf{f}}{\partial \mathbf{x}} = \begin{bmatrix} \mathbf{0} & \mathbf{I} \\ \mathbf{G} & \mathbf{0} \end{bmatrix}_{n \times n}, \qquad \mathbf{G} = \begin{bmatrix} \mathbf{G}_1 & \mathbf{0} & \mathbf{0} \\ \mathbf{0} & \ddots & \mathbf{0} \\ \mathbf{0} & \mathbf{0} & \mathbf{G}_p \end{bmatrix} \qquad (4)$$

where, for $j = 1, \ldots, p$,

$$\mathbf{G}_j := \frac{\partial \mathbf{g}_j}{\partial \mathbf{r}_j} = \frac{\mu}{\|\mathbf{r}_j\|^5}(3\mathbf{r}_j\mathbf{r}_j^T - \|\mathbf{r}_j\|^2\mathbf{I}) \qquad (5)$$

The Hessian matrix can be similarly partitioned as follows:

$$\frac{\partial^2 f_i}{\partial \mathbf{x}^2} = \begin{bmatrix} \boldsymbol{\Delta}_{f_i} & \mathbf{0} \\ \mathbf{0} & \mathbf{0} \end{bmatrix}_{n \times n} \qquad (6)$$

The matrix $\boldsymbol{\Delta}_{f_i} \in \mathbb{R}^{\frac{n}{2} \times \frac{n}{2}}$ is $\mathbf{0}$ for $i \leq n/2$, and sparse otherwise. In particular, for $i = n/2 + 3(j-1) + k > n/2$ the matrix $\boldsymbol{\Delta}_{f_i}$ has $\mathbf{0}$ submatrices everywhere except for the 3×3 nonzero submatrix in rows and columns $3j-2, 3j-1, 3j$ denoted $\mathbf{G}'_{jk}$ where

$$\mathbf{G}'_{jk} := \frac{\partial^2 g_{j_k}}{\partial \mathbf{r}_j^2} = \frac{3\mu}{\|\mathbf{r}_j\|^5}\left(\mathbf{r}_j\mathbf{I}_k^T + \mathbf{I}_k\mathbf{r}_j^T + r_{j_k}\mathbf{I} - 5r_{j_k}\frac{\mathbf{r}_j\mathbf{r}_j^T}{\|\mathbf{r}_j\|^2}\right) \quad (7)$$

The subscript j refers to the spacecraft number ($j = 1, \ldots, p$), the subscript k refers to the x, y, or z component of $\mathbf{v}_j$ or $\mathbf{g}_j$ ($k = 1, 2, 3$, respectively) corresponding to f_i, and $\mathbf{I}_k$ refers to the kth column of the 3×3 identity matrix $\mathbf{I}$.

For comparison, whenever a formation is examined, two measurement scenarios are considered. The first scenario involves the use of only the inertial[‡] range measurements from the three libration point tracking stations to each spacecraft ($m = m_{\text{in}} = 3p$). [When a single cluster of spacecraft ($p = 1$) is examined during the cislunar transfer segment, only the two equilateral stations are used and $m = 2$.] The second scenario employs inertial range measurements with the addition of m_{rel} relative range measurements between each spacecraft ($m = m_{\text{in}} + m_{\text{rel}}$ and $m_{\text{rel}} = p(p-1)/2$). Thus, the measurement model for $k = 1, \ldots, m$ where $1 \leq k \leq m_{\text{in}}$ refers to an inertial range measurement and $k > m_{\text{in}}$ refers to a relative range measurement can be constructed as

$$\mathbf{h}(\mathbf{x}) = [\, h_1 \quad \cdots \quad h_m \,]^T, \qquad h_k = \rho_{ij} = \|\boldsymbol{\rho}_{ij}\| \qquad (8)$$

where

$$\boldsymbol{\rho}_{ij} = \begin{cases} \mathbf{r}_j - \mathbf{r}_{s_i}, & 1 \leq k \leq m_{\text{in}} \\ \mathbf{r}_j - \mathbf{r}_i, & k > m_{\text{in}} \end{cases} \qquad (9)$$

The subscript j refers to the primary spacecraft number, whereas the subscript i refers to the station number (for inertial measurements) or the secondary spacecraft number (for relative measurements) that is tracking the primary. Consequently, $\mathbf{r}_{s_i}$ refers to the position vector of the ith tracking station, where i corresponds to the station number of L_4, L_5, or L_2.

To avoid potential numerical instabilities and to ensure that the complications when fusing relative measurements are not just the result of more accurate sensors (i.e., numerically small measurement noise), all inertial and relative range measurements are simulated using an identical measurement noise, which has a standard deviation of $\sigma_\rho = 5$ m. Likewise, unless otherwise stated, the filter uses the same corresponding measurement noise covariance (i.e., $\mathbf{R} = \sigma_\rho^2\mathbf{I}$, see Sec. III). All measurements are available simultaneously at equally spaced intervals, and, unless otherwise stated, the measurements are processed simultaneously the instant they become available. The cislunar transfer segment uses a measurement

---

[‡]Practically speaking, tracking station range measurements are also relative in that they are taken relative to a noninertial observer. However, for discussion purposes, the term "inertial range measurement" is used to refer to a range measurement taken from an observer with a known ephemeris in the inertial frame; whereas the term "relative range measurement" is reserved for a crosslink range measurement taken between spacecraft contained in the estimated state.

frequency of 1 h, whereas the lunar orbit segment uses a frequency of 1 min. Finally, because designing the logistics required to implement such a filter is not the objective of this research, it has been assumed here that the spacecraft can instantly exchange serial data messages containing the inertial and relative measurement information of the other spacecraft in the formation.

With the measurement model defined in Eq. (8), the derivation and computation of the Jacobian and Hessian matrices, which will later be required by the Kalman filter, can be obtained. In particular, reexamining Eq. (1) and noting that the measurements are not functions of velocity, the Jacobian matrix can be partitioned as

$$\frac{\partial \mathbf{h}}{\partial \mathbf{x}} = [\mathbf{\Theta}|0]_{m \times n} \quad \text{where } \mathbf{\Theta} := \begin{bmatrix} \frac{\partial \mathbf{h}}{\partial \mathbf{r}_1} & \cdots & \frac{\partial \mathbf{h}}{\partial \mathbf{r}_p} \end{bmatrix} \quad (10)$$

which has nonzero components

$$\frac{\partial h_k}{\partial \mathbf{r}_j} = \frac{\partial \rho_{ij}}{\partial \mathbf{r}_j} = +\frac{\boldsymbol{\rho}_{ij}^T}{\rho_{ij}} \quad \text{and} \quad \frac{\partial h_k}{\partial \mathbf{r}_i} = \frac{\partial \rho_{ij}}{\partial \mathbf{r}_i} = \begin{cases} \mathbf{0}^T & 1 \le k \le m_{\text{in}} \\ -\frac{\boldsymbol{\rho}_{ij}^T}{\rho_{ij}} & k > m_{\text{in}} \end{cases} \tag{11}$$

and zero components elsewhere. Partitioning the corresponding Hessian matrix results in

$$\frac{\partial^2 h_k}{\partial \mathbf{x}^2} = \begin{bmatrix} \mathbf{\Delta}_{h_k} & \mathbf{0} \\ \mathbf{0} & \mathbf{0} \end{bmatrix}_{n \times n} \tag{12}$$

The matrix $\mathbf{\Delta}_{h_k} \in \mathbb{R}^{\frac{n}{2} \times \frac{n}{2}}$ has $\mathbf{0}$ submatrices everywhere except for the 3×3 nonzero submatrix in rows and columns $3j-2$, $3j-1$, $3j$ denoted $\mathbf{\Theta}'_{ij}$,

$$\mathbf{\Theta}'_{ij} := \frac{\partial^2 \rho_{ij}}{\partial \mathbf{r}_j^2} = \frac{1}{\rho_{ij}^3} (\rho_{ij}^2 \mathbf{I} - \boldsymbol{\rho}_{ij} \boldsymbol{\rho}_{ij}^T) \tag{13}$$

The subscript j refers to the primary spacecraft number, whereas the subscript i refers to the station number (for inertial measurements) or the secondary spacecraft number (for relative measurements) that is tracking the primary. Finally, for relative measurements ($k > m_{\text{in}}$) the submatrix $\mathbf{\Theta}'_{ij}$ appears four times, due to the additional rows and columns $3i-2$, $3i-1$, $3i$, except the two off-diagonal submatrices are negative ($-\mathbf{\Theta}'_{ij}$).

III. Filter Algorithms

Two navigation algorithms are considered. The first algorithm is the continuous-discrete extended Kalman filter (EKF) (see Gelb [2] for more details). The EKF accommodates nonlinearities by using first-order Taylor series expansions to linearize system and measurement models about the current state estimate. The second algorithm is a variation of the EKF known as the modified Gaussian second-order filter (GSF) (see Maybeck [3] for more details). The GSF is an EKF that incorporates second-order terms of the Taylor series expansions in the linearization process. Although the GSF is only implemented in Sec. V.C, because the GSF can easily be reduced to the EKF by setting the second-order terms equal to zero, only the GSF algorithm is presented here, and the EKF follows directly. Finally, when possible without loss of clarity, functional dependencies on the state and time have been suppressed for compactness and readability.

A. General Models

The system model as a function of the state $\mathbf{x} \in \mathbb{R}^n$ has the form

$$\dot{\mathbf{x}}(t) = \mathbf{f}(\mathbf{x}(t), t) + \mathbf{w}(t) \tag{14}$$

with

$$E[\mathbf{w}(t)] = \mathbf{0} \quad \text{and} \quad E[\mathbf{w}(t)\mathbf{w}^T(\tau)] = \mathbf{Q}_{\text{spec}}\delta(t-\tau) \tag{15}$$

where $\delta(t-\tau)$ is the Dirac delta function. The nonlinear dynamic model $\mathbf{f}$ is assumed to be sufficiently differentiable. The process noise $\mathbf{w}(t)$ is modeled as a zero-mean white noise process with constant power spectral density $\mathbf{Q}_{\text{spec}} \in \mathbb{R}^{n \times n}$. The constant power spectral density implies that the stochastic process has infinite variance. This is an idealized concept that is not physically realizable, however, it does serve as a useful mechanism for modeling system uncertainties and disturbances. The matrix $\mathbf{Q}_{\text{spec}} \ge \mathbf{0}$ is a filter input. The noise $\mathbf{w}(t)$ represents those disturbances that are unmodeled because they are unknown, as well as those intentionally excluded due to model complexity or computational limitations. Consequently, in simulation, the true environment dynamics are not simulated by integrating the filter dynamic model plus noise as Eq. (14) would suggest, but instead by integrating an environment dynamic model that is of a higher fidelity than the filter dynamic model. Equation (14) is the model employed in the EKF design.

Similarly, the measurement model for the measurement vector $\mathbf{z} \in \mathbb{R}^m$ has the form

$$\mathbf{z}(t_d) = \mathbf{h}(\mathbf{x}(t_d)) + \mathbf{u}(t_d) \tag{16}$$

with

$$E[\mathbf{u}(t_d)] = \mathbf{0} \quad \text{and} \quad E[\mathbf{u}(t_c)\mathbf{u}^T(t_d)] = \mathbf{R}(t_d)\delta_{cd} \tag{17}$$

where δ_{cd} is the Kronecker delta. The nonlinear measurement model $\mathbf{h}$ is assumed to be sufficiently differentiable. The measurement noise $\mathbf{u}(t_d)$ is modeled as a zero-mean white noise sequence with noise covariance $\mathbf{R} \in \mathbb{R}^{m \times m}$. The matrix $\mathbf{R}$ is a filter input.

It is also assumed that the system and measurement noise are uncorrelated in time, that is,

$$E[\mathbf{w}(t)\mathbf{u}^T(t_d)] = \mathbf{0} \quad \forall \ t, t_d \tag{18}$$

The state estimate error $\mathbf{e}$ is defined as

$$\mathbf{e}(t) = \mathbf{x}(t) - \hat{\mathbf{x}}(t) \tag{19}$$

with

$$E[\mathbf{e}(t)] = \mathbf{0} \quad \text{and} \quad E[\mathbf{e}(t)\mathbf{e}^T(t)] = \mathbf{P}(t) \tag{20}$$

and the initial state estimate $\hat{\mathbf{x}}(t_0)$ is such that the initial state error $\mathbf{e}(t_0)$ is assumed zero-mean with covariance $\mathbf{P}(t_0)$. Because the computed state error covariance is only an approximation of the true state error covariance (in the nonlinear setting), the actual filter performance must be verified through Monte Carlo analysis.

B. State and State Error Covariance Propagation

The second-order state estimate is propagated between measurements using the dynamic model $\mathbf{f}$ such that

$$\dot{\hat{\mathbf{x}}}(t) = \mathbf{f}(\hat{\mathbf{x}}(t)) + \mathbf{b}_f(t), \qquad t_{d-1} \le t \le t_d \tag{21}$$

where $\mathbf{b}_f$ is the bias compensation term resulting from the inclusion of second-order terms. Consequently, if second-order terms are ignored, $\mathbf{b}_f = \mathbf{0}$ and Eq. (21) reduces to the standard state estimate propagation equation used by the EKF. The ith component of the bias term b_{f_i} can be written as a function of the state error covariance $\mathbf{P}$ as

$$b_{f_i}(t) = \tfrac{1}{2}\text{trace}(\mathbf{F}'_i(\hat{\mathbf{x}}(t))\mathbf{P}(t)), \qquad i = 1, \ldots, n \tag{22}$$

where $\mathbf{F}'_i$ is the Hessian of the ith component of the dynamic model f_i with respect to the state and evaluated at the current state estimate. The Jacobian $\mathbf{F}$ and Hessian $\mathbf{F}'_i$ are defined as follows:

$$\mathbf{F}(\hat{\mathbf{x}}(t)) := \frac{\partial \mathbf{f}}{\partial \mathbf{x}}\bigg|_{\mathbf{x}=\hat{\mathbf{x}}(t)} \in \mathbb{R}^{n \times n} \quad \text{and} \quad \mathbf{F}'_i(\hat{\mathbf{x}}(t)) := \frac{\partial^2 f_i}{\partial \mathbf{x}^2}\bigg|_{\mathbf{x}=\hat{\mathbf{x}}(t)} \in \mathbb{R}^{n \times n} \tag{23}$$

The state error covariance is then propagated between measurements by directly integrating

$$\dot{\mathbf{P}}(t) = \mathbf{F}(\hat{\mathbf{x}}(t))\mathbf{P}(t) + \mathbf{P}(t)\mathbf{F}^T(\hat{\mathbf{x}}(t)) + \mathbf{Q}_{\text{spec}}, \qquad t_{d-1} \le t \le t_d \tag{24}$$

with initial condition $\mathbf{P}(t_{d-1}) = \mathbf{P}(t_{d-1}^+)$ or by using the state transition matrix.

C. State and State Error Covariance Update

The state estimate and state error covariance are propagated until a measurement becomes available at time t_d. At t_d, the state estimate and state error covariance are updated by incorporating the measurement. Values immediately before the measurement update are referred to as a priori values and are denoted with a superscript "−." Conversely, values immediately after the measurement update are referred to as a posteriori values and are denoted with a superscript "+." Thus, the state estimate update at time t_d can be written as

$$\hat{\mathbf{x}}(t_d^+) = \hat{\mathbf{x}}(t_d^-) + \mathbf{K}(t_d)\boldsymbol{\epsilon}(t_d) \tag{25}$$

where $\mathbf{K}$ is the Kalman gain, $\boldsymbol{\epsilon}$ is the second-order measurement residual defined as

$$\boldsymbol{\epsilon}(t_d) := \mathbf{z}(t_d) - \mathbf{h}(\hat{\mathbf{x}}(t_d^-)) - \mathbf{b}_h(t_d) \tag{26}$$

and $\mathbf{b}_h$ is the bias compensation term resulting from the inclusion of second-order terms. The term $\mathbf{b}_h$ is absent in the first-order (EKF) formulation. The kth component of the bias term b_{h_k} can be written as a function of the state error covariance $\mathbf{P}$ as

$$b_{h_k}(t_d) = \tfrac{1}{2}\text{trace}(\mathbf{H}_k'(\hat{\mathbf{x}}(t_d^-))\mathbf{P}(t_d^-)), \qquad k = 1, \ldots, m \tag{27}$$

where $\mathbf{H}_k'$ is the Hessian of the kth component of the measurement model h_k with respect to the state and evaluated at the a priori state estimate. The Jacobian $\mathbf{H}$ and Hessian $\mathbf{H}_k'$ are defined as follows:

$$\mathbf{H}(\hat{\mathbf{x}}(t_d^-)) := \left.\frac{\partial \mathbf{h}}{\partial \mathbf{x}}\right|_{\mathbf{x}=\hat{\mathbf{x}}(t_d^-)} \in \mathbb{R}^{m \times n} \quad \text{and}$$

$$\mathbf{H}_k'(\hat{\mathbf{x}}(t_d^-)) := \left.\frac{\partial^2 h_k}{\partial \mathbf{x}^2}\right|_{\mathbf{x}=\hat{\mathbf{x}}(t_d^-)} \in \mathbb{R}^{n \times n} \tag{28}$$

The Kalman gain at time t_d is then given by

$$\mathbf{K}(t_d) = \mathbf{P}(t_d^-)\mathbf{H}^T(\hat{\mathbf{x}}(t_d^-))\mathbf{W}^{-1}(t_d) \tag{29}$$

where $\mathbf{W}$ is the measurement residual covariance defined as

$$\mathbf{W}(t_d) := \mathbf{H}(\hat{\mathbf{x}}(t_d^-))\mathbf{P}(t_d^-)\mathbf{H}^T(\hat{\mathbf{x}}(t_d^-)) + \mathbf{R}(t_d) + \mathbf{B}_h(t_d) \tag{30}$$

and $\mathbf{B}_h$ is an additional covariance term resulting from the inclusion of second-order terms. The jkth component ($j = 1, \ldots, m$) of the covariance term $B_{h_{jk}}$ can be written as a function of the state error covariance $\mathbf{P}$ as follows:

$$B_{h_{jk}}(t_d) = \tfrac{1}{2}\text{trace}(\mathbf{H}_j'(\hat{\mathbf{x}}(t_d^-))\mathbf{P}(t_d^-)\mathbf{H}_k'(\hat{\mathbf{x}}(t_d^-))\mathbf{P}(t_d^-)) \tag{31}$$

Once the Kalman gain has been computed, the state error covariance is also updated at time t_d using the Joseph formula:

$$\mathbf{P}(t_d^+) = [\mathbf{I} - \mathbf{K}(t_d)\mathbf{H}(\hat{\mathbf{x}}(t_d^-))]\mathbf{P}(t_d^-)[\mathbf{I} - \mathbf{K}(t_d)\mathbf{H}(\hat{\mathbf{x}}(t_d^-))]^T$$
$$+ \mathbf{K}(t_d)\mathbf{R}(t_d)\mathbf{K}^T(t_d) \tag{32}$$

The state error covariance is resymmetrized after the update. Finally, note that, once again, if the second-order terms are ignored, that is, if $\mathbf{b}_h = \mathbf{0}$ and $\mathbf{B}_h = \mathbf{0}$, then Eqs. (25), (29), and (32) reduce to the standard update equations used by the EKF.

IV. Navigation Observability Analysis

By examining the observability measure associated with the observer locations and formation geometry, it is possible to develop guidelines that not only predict the expected navigation performance of a particular geometry but also which geometries should be avoided

Table 1 Lunar mission cases

Case	Spacecraft	n	Measurement profile	and frequency	m
0	1	4	Inertial only	Every hour	2
1.0	2	12	Inertial only	Every minute	6
1.1	2	12	Relative fusion	Every minute	7
2.0	6	36	Inertial only	Every minute	18
2.1	6	36	Relative fusion	Every minute	33

entirely. To this end, three mission cases have been examined: cases 0, 1, and 2 in Table 1. As outlined in Sec. II, case 0 examines a cluster of spacecraft on a cislunar transfer trajectory, whereas cases 1 and 2 examine two formation variations in a circular polar orbit about the moon. Cases x.0 and x.1 are identical (including noise values) with the sole exception that the x.0 cases use only inertial measurements, and the x.1 cases fuse inertial and relative measurements. All three cases are initialized using a moderate level of initial covariance (position $\sigma_r \sim 10^{-1}$ km and velocity $\sigma_v \sim 10^{-5}$ km/s).

A. Observability Condition

In a sense, observability measures the ability to estimate the state at time t using measurements of the output of the system. More explicitly, the state space of a system is said to be observable if and only if, for any unknown initial state there exists a finite time such that knowledge of the input and the output over that finite time suffices to determine uniquely the initial state [4].

In other words, a useful measure of observability should provide a sense of the ability to obtain an estimate of the state vector $\mathbf{x} \in \mathbb{R}^n$ given the time history of the measurement vector $\mathbf{z} \in \mathbb{R}^m$. The most common measures of observability are associated with the properties of the linear time-invariant (LTI) observability matrix $\mathcal{O}$,

$$\mathcal{O} = [\mathbf{H}^T \quad (\mathbf{HF})^T \quad (\mathbf{HF}^2)^T \quad \cdots \quad (\mathbf{HF}^{n-1})^T]_{nm \times n}^T \tag{33}$$

In particular, a continuous deterministic nth-order, LTI system is said to be *locally* observable if, and only if, the matrix $\mathcal{O}$ has rank n (which is equivalent to $\mathcal{O}$ having n linearly independent rows) [2,5]. Furthermore, $\mathcal{O}$ has rank n if, and only if, $\det(\mathcal{O}^T\mathcal{O})^{1/2} \ne 0$ [4]. Thus, the condition for observability is that the observability measure $\det(\mathcal{O}^T\mathcal{O})^{1/2}$ be nonzero.

Although the systems examined in this paper are neither linear nor time invariant, by defining $\mathbf{F}$ and $\mathbf{H}$ as the evaluation of Eqs. (23) and (28) on some nominal or reference trajectory at a "frozen" instant in time, examination of the LTI observability measure can still provide useful insight into the local observability of the systems at that time. However, because in doing so the time-invariant observability measure is examined at essentially independent instances in time, it should be noted that the measure will not account for any observability gained from a buildup of measurement information. Thus, the time-invariant analysis is typically most applicable during early portions of the navigation.

B. Cluster-Observer Geometry

In the cislunar transfer mission segment, case 0, a single cluster of spacecraft is tracked in two-dimensional space ($n = 4$) using two tracking stations ($m = 2$) located at each of the two equilateral libration points (L_4 and L_5). Recalling Eqs. (4) and (10),

$$\mathbf{F} = \begin{bmatrix} \mathbf{0} & \mathbf{I} \\ \mathbf{G} & \mathbf{0} \end{bmatrix}, \qquad \mathbf{H} = \begin{bmatrix} \boldsymbol{\rho}_1^T/\rho_1 & \mathbf{0}^T \\ \boldsymbol{\rho}_2^T/\rho_2 & \mathbf{0}^T \end{bmatrix} \tag{34}$$

which results in the following observability matrix:

$$
\mathcal{O} = \begin{bmatrix}
\boldsymbol{\rho}_1^T/\rho_1 & \mathbf{0}^T \\
\boldsymbol{\rho}_2^T/\rho_2 & \mathbf{0}^T \\
\mathbf{0}^T & \boldsymbol{\rho}_1^T/\rho_1 \\
\mathbf{0}^T & \boldsymbol{\rho}_2^T/\rho_2 \\
\boldsymbol{\rho}_1^T \mathbf{G}/\rho_1 & \mathbf{0}^T \\
\boldsymbol{\rho}_2^T \mathbf{G}/\rho_2 & \mathbf{0}^T \\
\mathbf{0}^T & \boldsymbol{\rho}_1^T \mathbf{G}/\rho_1 \\
\mathbf{0}^T & \boldsymbol{\rho}_2^T \mathbf{G}/\rho_2
\end{bmatrix} \qquad (35)
$$

Because the cluster is treated as one spacecraft, the j subscript is dropped for convenience.

At this point, it is useful to consider the magnitude of the matrix $\mathbf{G}$. In particular, because $\mathbf{G}$ is symmetric, its 2-norm is the maximum of the absolute value of its eigenvalues. Thus, analytically computing the eigenvalues of $\mathbf{G}$ results in

$$
\lambda(\mathbf{G}) = \frac{\mu}{\|\mathbf{r}\|^3} \begin{bmatrix} -1 \\ -1 \\ 2 \end{bmatrix} \quad \text{and} \quad \|\mathbf{G}\| = \max|\lambda(\mathbf{G})| = \frac{2\mu}{\|\mathbf{r}\|^3} \quad (36)
$$

where here μ is the gravitational constant of the Earth. Therefore, because $\|\mathbf{r}\|$ is always greater than the radius of the Earth, at most $\|\mathbf{G}\| < 3.07 \times 10^{-6} \ 1/s^2$ and, at the end of the transfer, $\|\mathbf{G}\| = 1.40 \times 10^{-11} \ 1/s^2$. Consequently, for simplification, these terms are considered negligible when examining the observability matrix analytically [however, not when computing the observability measure $\det(\mathcal{O}^T\mathcal{O})^{1/2}$ numerically]. This implies that $\mathcal{O}$ approximately only contains the rows resulting from $\mathbf{H}$ and $\mathbf{HF}$. Since $n = 4$, the remaining four rows of $\mathcal{O}$ must all be linearly independent to satisfy the observability condition. Examining $\mathcal{O}$ leads to the conclusion that, if $\boldsymbol{\rho}_1$ and $\boldsymbol{\rho}_2$ are parallel, the number of linearly independent rows is reduced to two and thus the observability condition is violated.

This can be illustrated both numerically and geometrically. Numerically, this can be detected by computing the observability measure, as seen in Fig. 3a. Recall that the observability condition is violated when the observability measure $\det(\mathcal{O}^T\mathcal{O})^{1/2} = 0$. Geometrically, the observability violation occurs when the spacecraft cluster crosses a line connecting the two tracking stations. Figure 3b shows the complete (transfer and return) cislunar trajectory with the Earth at the origin, the trajectory of the moon, and libration points L_4 and L_5 at two discrete times. In particular, the times where an event occurs in Fig. 3a are also indicated on the trajectory in Fig. 3b. At each of these times, the line connecting the L_4 tracking station and the L_5 tracking station intersects the transfer trajectory at the current location of the spacecraft cluster, thus indicating that, as predicted, both range vectors are parallel.

The corresponding navigation state error can be seen in Fig. 4. Notice that the bulges in covariance occurring around 1.5 days coincide with the violation of the observability condition, as seen in Fig. 3a. As seen in Fig. 5, the residuals are approximately zero-mean, white noise with a standard deviation of about 5 m, which is an indication that the filter is working properly.

Via simulation, it has been shown that examination of the observability condition can help detect potential problems in the navigation performance. In particular, for this scenario, the two-dimensional system becomes unobservable when the range vectors are parallel. The next two mission cases extend this concept to three-dimensional space while also examining the advantages and complexities of adding additional spacecraft.

C. Formation-Observer Geometry

In the lunar orbit mission segment, cases 1 and 2, the cluster separates and a formation of spacecraft is tracked in three-dimensions using three tracking stations, with two located at each of the equilateral libration points (L_4 and L_5) and one at the colinear
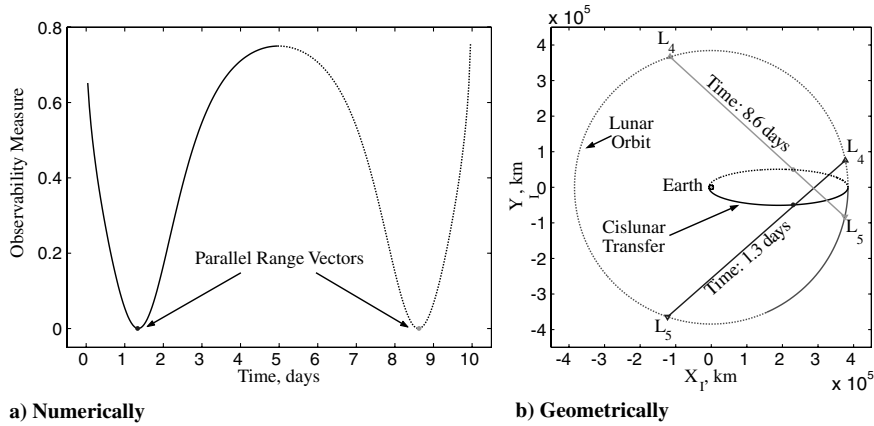

a) Numerically   b) Geometrically

Fig. 3   Detection of reduced observability for case 0.

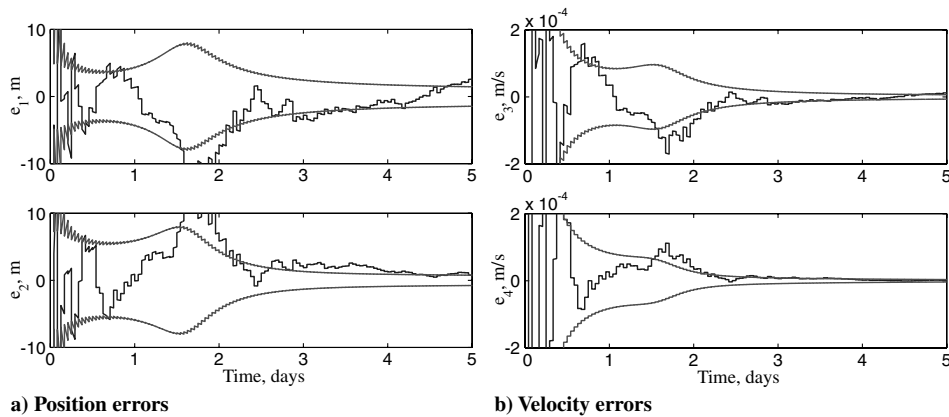a) Position errors   b) Velocity errors

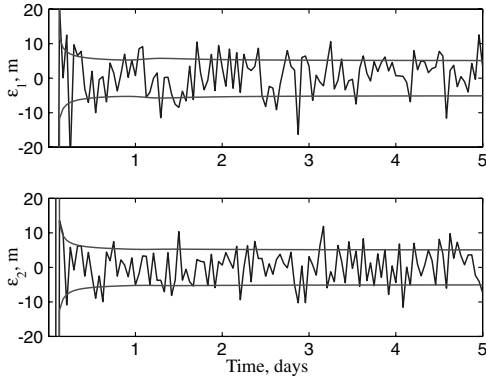**Fig. 4   Time history of the inertial state errors for case 0.**

Fig. 5 Time history of the residuals for case 0.

libration point on the far side of the moon (L_2). As seen in Table 1, each mission examines two measurement scenarios: without (x.0) and with (x.1) the use of relative range measurements. For all cases, the dynamics matrix $\mathbf{F}$ is defined using Eq. (4).

Applying Eq. (10), the mapping matrix $\mathbf{H}$ for case 1.1 is given by

$$\mathbf{H} = \begin{bmatrix} \boldsymbol{\rho}_{11}^T/\rho_{11} & \mathbf{0}^T & \mathbf{0}^T & \mathbf{0}^T \\ \boldsymbol{\rho}_{21}^T/\rho_{21} & \mathbf{0}^T & \mathbf{0}^T & \mathbf{0}^T \\ \boldsymbol{\rho}_{31}^T/\rho_{31} & \mathbf{0}^T & \mathbf{0}^T & \mathbf{0}^T \\ \mathbf{0}^T & \boldsymbol{\rho}_{12}^T/\rho_{12} & \mathbf{0}^T & \mathbf{0}^T \\ \mathbf{0}^T & \boldsymbol{\rho}_{22}^T/\rho_{22} & \mathbf{0}^T & \mathbf{0}^T \\ \mathbf{0}^T & \boldsymbol{\rho}_{32}^T/\rho_{32} & \mathbf{0}^T & \mathbf{0}^T \\ -\boldsymbol{\rho}_{12}^T/\rho_{12} & \boldsymbol{\rho}_{12}^T/\rho_{12} & \mathbf{0}^T & \mathbf{0}^T \end{bmatrix} \quad (37)$$

where the additional spacing is used to partition and distinguish between inertial measurement rows ($1 \leq k \leq m_{\text{in}} = 6$) and relative measurement rows ($k > m_{\text{in}} = 6$). [This distinction is important because, as defined in Eq. (9), inertial range ρ_{ij} is not the same as relative range ρ_{ij}. However, this commonality allows for generalized equations and analysis.] Although the full observability matrix is too large to present here, the terms of Eq. (33) can be found for $i = 0, 1, \ldots, n - 1$, such that, if i is zero or even, it follows that

$$\mathbf{H}\,\mathbf{F}^i = \begin{bmatrix} \boldsymbol{\rho}_{11}^T\mathbf{G}_1^{i/2}/\rho_{11} & \mathbf{0}^T & \mathbf{0}^T & \mathbf{0}^T \\ \boldsymbol{\rho}_{21}^T\mathbf{G}_1^{i/2}/\rho_{21} & \mathbf{0}^T & \mathbf{0}^T & \mathbf{0}^T \\ \boldsymbol{\rho}_{31}^T\mathbf{G}_1^{i/2}/\rho_{31} & \mathbf{0}^T & \mathbf{0}^T & \mathbf{0}^T \\ \mathbf{0}^T & \boldsymbol{\rho}_{12}^T\mathbf{G}_2^{i/2}/\rho_{12} & \mathbf{0}^T & \mathbf{0}^T \\ \mathbf{0}^T & \boldsymbol{\rho}_{22}^T\mathbf{G}_2^{i/2}/\rho_{22} & \mathbf{0}^T & \mathbf{0}^T \\ \mathbf{0}^T & \boldsymbol{\rho}_{32}^T\mathbf{G}_2^{i/2}/\rho_{32} & \mathbf{0}^T & \mathbf{0}^T \\ -\boldsymbol{\rho}_{12}^T\mathbf{G}_1^{i/2}/\rho_{12} & \boldsymbol{\rho}_{12}^T\mathbf{G}_2^{i/2}/\rho_{12} & \mathbf{0}^T & \mathbf{0}^T \end{bmatrix} \quad (38)$$

and if i is odd, it follows that

$$\mathbf{H}\,\mathbf{F}^i = \begin{bmatrix} \mathbf{0}^T & \mathbf{0}^T & \boldsymbol{\rho}_{11}^T\mathbf{G}_1^{(i-1)/2}/\rho_{11} & \mathbf{0}^T \\ \mathbf{0}^T & \mathbf{0}^T & \boldsymbol{\rho}_{21}^T\mathbf{G}_1^{(i-1)/2}/\rho_{21} & \mathbf{0}^T \\ \mathbf{0}^T & \mathbf{0}^T & \boldsymbol{\rho}_{31}^T\mathbf{G}_1^{(i-1)/2}/\rho_{31} & \mathbf{0}^T \\ \mathbf{0}^T & \mathbf{0}^T & \mathbf{0}^T & \boldsymbol{\rho}_{12}^T\mathbf{G}_2^{(i-1)/2}/\rho_{12} \\ \mathbf{0}^T & \mathbf{0}^T & \mathbf{0}^T & \boldsymbol{\rho}_{22}^T\mathbf{G}_2^{(i-1)/2}/\rho_{22} \\ \mathbf{0}^T & \mathbf{0}^T & \mathbf{0}^T & \boldsymbol{\rho}_{32}^T\mathbf{G}_2^{(i-1)/2}/\rho_{32} \\ \mathbf{0}^T & \mathbf{0}^T & -\boldsymbol{\rho}_{12}^T\mathbf{G}_1^{(i-1)/2}/\rho_{12} & \boldsymbol{\rho}_{12}^T\mathbf{G}_2^{(i-1)/2}/\rho_{12} \end{bmatrix} \quad (39)$$

Equations (37–39) for case 1.0 can easily be obtained by removing the relative measurement row (i.e., the bottom row).

Once again, it should be noted that the terms containing $\mathbf{G}$ are relatively small. In particular, because the spacecraft are in 100-km-altitude circular orbits about the moon, it follows that $\|\mathbf{G}\| = 1.58 \times 10^{-6} \ 1/s^2$. Additionally, due to the increased dimension of the state, the observability matrix now contains powers of $\mathbf{G}$, which leads to even smaller contributions. Consequently, these terms are again

considered negligible when examining the observability matrix analytically [however, not when computing the observability measure $\det(\mathcal{O}^T\mathcal{O})^{1/2}$ numerically]. This implies that $\mathcal{O}$ approximately only contains the rows resulting from $\mathbf{H}$ and $\mathbf{HF}$.

First consider the terms $\mathbf{H}$ and $\mathbf{HF}$ for case 1.0 (inertial measurements only). If any inertial range vectors to the *same*[§] spacecraft are parallel, the corresponding set of rows of the observability matrix is linearly dependent. This implies that the set contributes only one linearly independent row. With the addition of a third tracking station, this result can be further extended. Because any two linearly independent vectors in $\mathbb{R}^3$ form the basis for a plane, any other vector that lies in this plane is linearly dependent on the basis vectors [6]. Consequently, if three or more inertial range vectors to the same spacecraft lie in the same plane, the corresponding set of rows of the observability matrix is linearly dependent. This implies that the set contributes only two linearly independent rows.

Now, reconsider the terms $\mathbf{H}$ and $\mathbf{HF}$ for case 1.1 (fused relative measurement). Notice that now if any inertial range vectors to two *different*[¶] spacecraft are parallel, and the relative range vector between these two spacecraft is also parallel, then the corresponding set of rows of the observability matrix is linearly dependent. This implies that this set of three contributes only two linearly independent rows. In other words, this particular relative measurement is not contributing to the observability of the state. This result can also be extended. Suppose that inertial range vectors from two stations to one spacecraft form a plane, and two more inertial range vectors to a different spacecraft form another plane. If the two planes are coplanar, the relative range vector between these two spacecraft must also lie in this plane because it has a point in each plane (located at each spacecraft). Therefore, these five range vectors are coplanar and the corresponding set of rows of the observability matrix is linearly dependent. Similarly, if these two planes are not coplanar, but the relative range vector between these two spacecraft lies along the intersection of these two planes, then the corresponding set of rows of the observability matrix is again linearly dependent. In both instances, the set of five contributes only four linearly independent rows. Once again, this implies that this particular relative measurement is not contributing to the observability of the state.

Figure 6 illustrates the detection of these events both numerically and geometrically. In particular, the times where events occurs in Fig. 6a are also indicated on the trajectory in Fig. 6b. However, although the detection of these events may cause reductions in observability, they do not necessarily indicate a complete loss of observability (i.e., the number of linearly independent rows of the observability matrix may still be n). This is especially important to remember considering the simplification made that rows containing $\mathbf{G}$ are negligible.

Recall that all three tracking stations lie in the same plane (X_I-Y_I plane). If the trajectory of the spacecraft also remained in the X_I-Y_I plane, all range vectors would lie in the same plane for all time and, according to the geometric analysis ($\mathbf{G}_j \approx \mathbf{0}$), the observability condition would be violated for all time and the z component of position would be unobservable. It is no coincidence that this mission segment examines a polar orbit. Because the orbit is perpendicular to the X_I-Y_I plane, it allows for maximum out-of-plane (Z_I) position for a given altitude. However, despite the chosen trajectory, there are still two points of concern. First, as seen in Fig. 6a near times 0.5 h and 1.5 h, there is still a considerable reduction in observability when the trajectory crosses the X_I-Y_I plane. Second, because the tracking

---

[§]The inertial range vectors must be to the same spacecraft because inertial range terms for different spacecraft are contained in different columns of the observability matrix; consequently, rows involving different spacecraft are always linearly independent.

[¶]The inertial range vectors must now be to two different spacecraft because relative range (between these two spacecraft) terms occur in the same columns of the observability matrix as the inertial range terms of the two spacecraft; consequently, two different spacecraft are required to span the columns of the rows containing relative range terms.
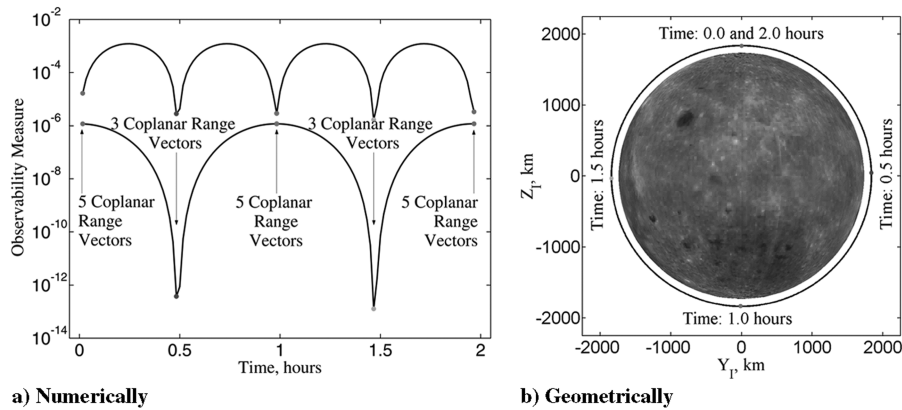
a) Numerically   b) Geometrically

Fig. 6   Detection of reduced observability for case 1.0 (lower curve) and case 1.1 (upper curve).

stations are distant relative to the distance that the trajectory travels out of plane, the inertial range vectors nearly lie in the same plane. Consequently, due to this lack of observability in the z component, the value of $\det(\mathcal{O}^T \mathcal{O})^{1/2}$ in the three-dimensional problem remains small relative to that of the two-dimensional cislunar problem.

Figure 6a illustrates the increase in observability due to the addition of a relative measurement. Notice that, when the relative measurement is included, the observability measure is always greater than it is without the relative measurement. Also, notice that, near times 0, 1, and 2 h, the observability measure for both cases 1.0 and 1.1 is roughly the same. This is expected because of the aforementioned event occurring at these times. Namely, the event in which the planes created by the inertial range vectors to two spacecraft are coplanar, thus resulting in five coplanar range vectors.
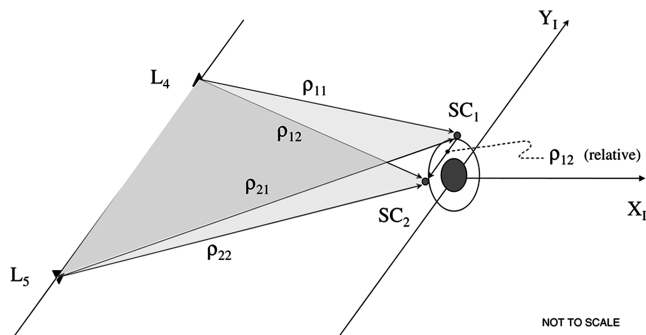

Fig. 7   Geometrical detection for case 1.

Figure 7 illustrates that these events occur when both spacecraft are near the "top" and "bottom" of the orbit. To be more exact, the relative range vector between the two spacecraft is parallel with the Y_I axis, which, more importantly, is also (initially) parallel with a line connecting the L_4 and L_5 tracking stations. This implies that the plane created by the L_4 and L_5 inertial range vector to the first spacecraft is (nearly) coplanar with the plane created by the L_4 and L_5 inertial range vector to the second spacecraft. Therefore, as described earlier, the relative range measurement row in the observability matrix is a linear combination of the four tracking station rows. Consequently, the relative measurement contributes no additional information and case 1.1 is essentially reduced to case 1.0.

As expected, all residuals are again approximately zero-mean, white noise with a standard deviation of about 5 m, similar to what was seen in Fig. 5. The navigation state error for the first spacecraft in case 1.0 can be seen in Fig. 8. The bulges in the state estimate error covariance occurring just before 1.5 h roughly coincide with the violation of the observability condition, as seen in Fig. 6a. Also notice that the largest position errors are in the Z_I direction. This is not surprising considering that all the inertial tracking stations are located in the X_I-Y_I plane. Consequently, as discussed later, the ability of the relative measurement to be out-of-plane yields the largest reduction in the navigation error of the Z_I position component.

Plots for the second spacecraft, as well as for case 1.1, are not presented here as they look very similar to Fig. 8. Despite this similarity, by examining the state error covariance that bounds the state error at the final time t_f for cases 1.0 and 1.1, as seen in Table 2, notice that there is a slight reduction in navigation error due to fusing the relative measurements. In particular, there is roughly a 15%
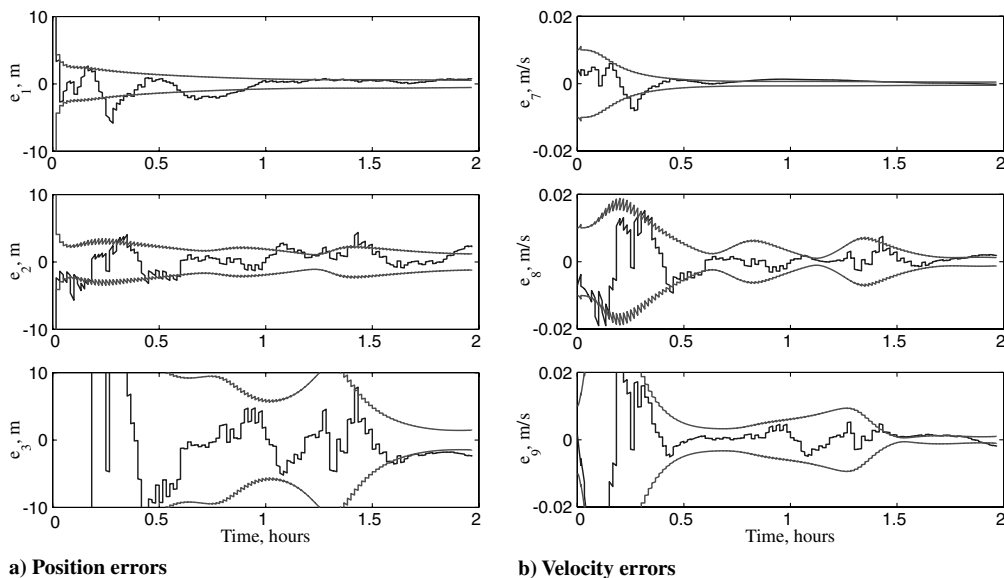

a) Position errors   b) Velocity errors

Fig. 8   Time history of the inertial state errors for case 1.0.

Table 2 Mission cases performance comparison

Case	$\bar{P}_{xx}^{1/2}(t_f)$, m	$\bar{P}_{yy}^{1/2}(t_f)$, m	$\bar{P}_{zz}^{1/2}(t_f)$, m	$\bar{P}_{\dot{x}\dot{x}}^{1/2}(t_f)$, mm/s	$\bar{P}_{\dot{y}\dot{y}}^{1/2}(t_f)$, mm/s	$\bar{P}_{\dot{z}\dot{z}}^{1/2}(t_f)$, mm/s
1.0	0.532	1.161	1.450	0.473	1.219	0.977
1.1	0.531	0.974	1.067	0.473	0.890	0.816
2.0	0.532	1.161	1.450	0.473	1.218	0.977
2.1	0.363	0.800	0.675	0.353	0.550	0.668

reduction in the y and $\dot{z}$ components, roughly a 25% reduction in the z and $\dot{y}$ components, but essentially no change in the x and $\dot{x}$ components. These reductions are relatively small for a few reasons. First, only one relative measurement is available. As will be shown later, additional relative measurements can lead to larger reductions in navigation error. Second, because three inertial measurements are used, there is already a high degree of observability without the relative measurements. Consequently, the navigation error is mostly driven by the inertial measurements. However, it has also been shown that a four-spacecraft formation using only one inertial measurement can achieve about a 50% reduction in the navigation errors of all components when fusing the six available relative measurements [7]. Finally, the lack of change of the components in the X_I direction is an expected result of the geometry. Because all the relative measurements are in the Y_I-Z_I plane, they do not contribute any information about the X_I direction.

Case 1 illustrates how the geometry of a problem can affect observability. It also demonstrates that relative measurements can be used to decrease inertial navigation error. Case 2 extends this concept further by examining the advantages and complexities of using multiple relative measurements. For case 2, the system dynamics matrix $\mathbf{F}$ and the measurement mapping matrix $\mathbf{H}$ are defined using Eqs. (4) and (10), respectively. Although the full measurement mapping matrix and observability matrix $\mathcal{O}$ for case 2 are too large to present here, they are very similar to those described in Eqs. (37–39) for case 1. Moreover, the case 2 observability matrix shares all of the reduced observability events presented in case 1. Likewise, due to the magnitude of $\|\mathbf{G}\|$, for simplification, terms containing $\mathbf{G}$ are again considered negligible when examining the observability matrix analytically [however, not when computing the observability measure $\det(\mathcal{O}^T\mathcal{O})^{1/2}$ numerically]. This again implies that $\mathcal{O}$ essentially only contains the rows resulting from $\mathbf{H}$ and $\mathbf{HF}$.

Examining $\mathbf{H}$ shows that the addition of multiple relative measurements yields an additional reduced observability event. In particular, consider the rows containing relative measurement terms between any three spacecraft. If any two relative range vectors between these three spacecraft are parallel, the third must also be parallel (i.e., the spacecraft are collinear). Consequently, the corresponding set of rows of the observability matrix is linearly dependent. Therefore, this set of three contributes only two linearly independent rows, which implies that one of the relative measurements is not contributing to the observability of the state.

Although the formation in case 2 was chosen such that this event does not occur, the events described in case 1 still do occur. The

numerical detection of these events in case 2 are illustrated in Fig. 9, although, because the additional planes of case 2 are nearly coplanar with the plane of case 1, Fig. 6b is still valid for the geometrical detection.

Figure 9 illustrates the dramatic increase in observability due to the relative measurements. Notice that the addition of multiple relative measurements now compensates for the loss of observability during the X_I-Y_I plane crossing. Also, although reductions in observability still do occur near the top and bottom of the orbits, as in case 1.1, case 2.1 is never fully reduced to case 2.0 because of the use of multiple relative measurements.

Again, as expected, all the residuals are approximately zero-mean, white noise with a standard deviation of about 5 m, similar to what was seen in Fig. 5. The navigation state error plots for case 2.0 are not presented here as they look very similar to what was seen in Fig. 8. In fact, as seen in Table 2, the average of the final state error covariance for all six spacecraft for case 2.0 is essentially the same as case 1.0. This is to be expected though because, without the use of relative measurements, the navigation of each spacecraft is essentially an independent, yet similar problem. When the relative measurements are added, however, the reduction in navigation error for case 2.1 is quite noticeable. In particular, Table 2 shows roughly a 55% reduction in the z and $\dot{y}$ components and roughly a 30% reduction in all other components. Also, notice that, unlike case 1.1, case 2.1 has a reduction in the X_I direction. This reduction in the X_I direction is the direct result of relative measurements taken out of the Y_I-Z_I plane.

Also, as seen in Figs. 10, there is an overall reduction in the magnitudes of the state estimate error covariance bulges, and an apparent increase in the rate of convergence, especially in the z and $\dot{y}$ components. In particular, for the z components covariance to converge to less than the measurement noise of 5 m, cases 1.0 and 2.0 required 90 measurement updates, case 1.1 required 54 measurement updates, and case 2.1 required only 28 measurement updates (updates occur every minute).

D. Summary of Observability Simulation Results

The relationship between observer geometry and the navigation performance of the EKF has been examined for several different mission cases. Using the LTI observability condition, possible reductions in observability were examined when using inertial range measurements due to the following geometric anomalies: 1) one spacecraft and the two or more stations tracking it are collinear, and 2) one spacecraft and the three or more stations tracking it are coplanar. These results were then expanded to include the use of relative range measurements and presented the following additional geometric anomalies: 3) two spacecraft and the station(s) tracking each are collinear, 4) the line connecting two spacecraft is parallel to the line connecting the two stations tracking each spacecraft (see Fig. 7), and 5) three spacecraft are collinear.

V. Relative Range Measurement Fusion

In the presence of large state error covariances, fusing** relative range measurements with inertial range measurements can cause an otherwise convergent filter (using inertial range measurements only) to diverge. To illustrate the complications involved in fusing relative
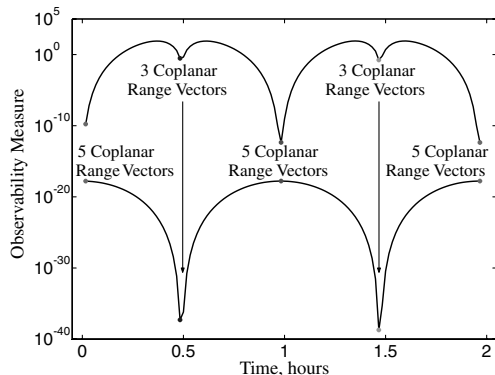

Fig. 9 Numerical detection of reduced observability for case 2.0 (lower curve) and case 2.1 (upper curve).

**Because by formulation the EKF fuses all measurements into a unified measurement vector, practically speaking, measurement fusion occurs between all measurements. However, for discussion purposes, the terms "fusing" and "fusion" are used to refer specifically to the combining of a set of inertial measurements with a set of relative measurements.

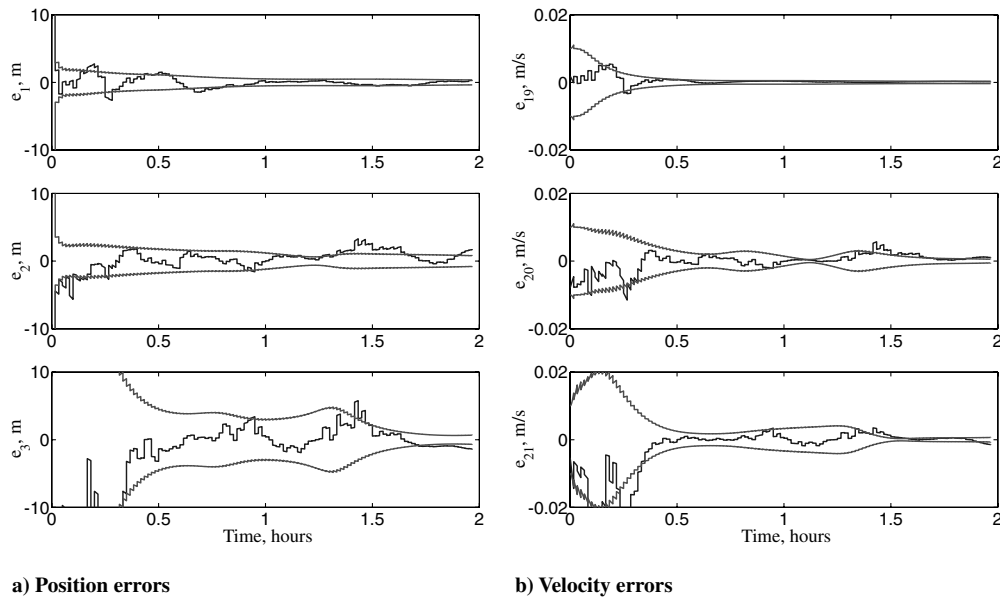a) Position errors　　　　　　　　　　　　　　　b) Velocity errors

Fig. 10　Time history of the inertial state errors for case 2.1.

and inertial range measurements, the six-spacecraft lunar orbit mission has been considered for two different state error covariance levels: moderate (case 2) and severe (case 3). The magnitudes of these levels of state error covariance are presented in Table 3.

After examining the complications associated with this type of measurement fusion, several robustness enhancement schemes are considered for fusing measurements in the presence of a severe level of state error covariance. These schemes, which range from some commonly used first-order numerical methods to second-order analytical methods, include the following: Scheme 0) no robustness enhancement scheme (EKF), scheme I) first-order methods (EKF) [scheme I-A) scalar update scheme, scheme I-B) process noise scheme, scheme I-C) measurement noise scheme, scheme I-D) selective measurement scheme], and scheme II) second-order methods (GSF).

After reviewing the performance of the first-order methods, the algorithms of the second-order method are investigated to determine their potential contribution to solving the challenges of fusing inertial and relative range measurements. All first-order methods are based on the standard EKF equations, whereas the GSF is used as the basis for the second-order methods.

A.　Fusion Complications

Using the initial state error covariance described in Table 3, the following test results are obtained:

1) The EKF converges for a moderate level of covariance when only inertial range measurements are used (case 2.0).

2) The EKF converges for a moderate level of covariance when fusing relative measurements (case 2.1).

3) The EKF converges for a severe level of covariance when only inertial measurements are used (case 3.0).

4) The EKF *diverges* for a severe level of covariance when fusing relative measurements (case 3.1).Table 4 summarizes these test cases and results.

These results beg the question, what is occurring in case 3.1 that causes the filter to be overly sensitive to the fusion of relative measurements? Or more precisely, why are the nonlinearities of the relative measurements much more significant than the inertial measurements? One response to these questions is to examine the

relationship between the state error covariance and the relative measurement residuals and residual covariances. Based on the state described in Eq. (1), the state error covariance is of the form

$$\mathbf{P} = \begin{bmatrix} \mathbf{P}_{rr} & \mathbf{P}_{rv} \\ \mathbf{P}_{vr} & \mathbf{P}_{vv} \end{bmatrix} \quad \text{where } \mathbf{P}_{vr}^T = \mathbf{P}_{rv} = \begin{bmatrix} \mathbf{P}_{r_1 v_1} & \cdots & \mathbf{P}_{r_1 v_p} \\ \vdots & \ddots & \vdots \\ \mathbf{P}_{r_p v_1} & \cdots & \mathbf{P}_{r_p v_p} \end{bmatrix} \tag{40}$$

and

$$\mathbf{P}_{rr} = \begin{bmatrix} \mathbf{P}_{r_1 r_1} & \cdots & \mathbf{P}_{r_1 r_p} \\ \vdots & \ddots & \vdots \\ \mathbf{P}_{r_p r_1} & \cdots & \mathbf{P}_{r_p r_p} \end{bmatrix} \quad \text{and}$$

$$\mathbf{P}_{vv} = \begin{bmatrix} \mathbf{P}_{v_1 v_1} & \cdots & \mathbf{P}_{v_1 v_p} \\ \vdots & \ddots & \vdots \\ \mathbf{P}_{v_p v_1} & \cdots & \mathbf{P}_{v_p v_p} \end{bmatrix} \tag{41}$$

The relative position error covariance between the ith and jth spacecraft can be written as

$$\mathbf{P}_{r_i r_j}^{\text{rel}} = \mathbf{P}_{r_i r_i} + \mathbf{P}_{r_j r_j} - \mathbf{P}_{r_i r_j} - \mathbf{P}_{r_j r_i} \tag{42}$$

It is also convenient to define a generic position covariance $\mathbf{P}_{\text{pos}}$ that is unique to each measurement type yielding

$$\mathbf{P}_{\text{pos}} := \begin{cases} \mathbf{P}_{r_j r_j} & 1 \leq k \leq m_{\text{in}} \\ \mathbf{P}_{r_i r_j}^{\text{rel}} & k > m_{\text{in}} \end{cases} \tag{43}$$

Recalling Eq. (30), it follows that Eq. (43) can be used to obtain a generic expression for the residual covariance of any range measurement (inertial or relative). In particular, the EKF residual covariance for measurement $h_k = \rho_{ij}$ (for any k) is

Table 3　State estimate error covariance levels

Level	Position, km	Velocity, km/s
Moderate	$\sigma_r \sim 10^{-1}$	$\sigma_v \sim 10^{-5}$
Severe	$\sigma_r \sim 10^{+1}$	$\sigma_v \sim 10^{-3}$

Table 4　Fusion simulation test cases

Case	Covariance level	Measurement profile	Filter performance
2.0	Moderate	Inertial only	Converges
2.1	Moderate	Relative fusion	Converges
3.0	Severe	Inertial only	Converges
3.1	Severe	Relative fusion	Diverges

$$W_{kk}^{\text{EKF}} = \frac{\boldsymbol{\rho}_{ij}^T \mathbf{P}_{\text{pos}}^- \boldsymbol{\rho}_{ij}}{\rho_{ij}^2} + R_{kk} \qquad (44)$$

Since $\mathbf{P}_{\text{pos}}^-$ is positive definite symmetric, by definition the quadratic ratio term in Eq. (44) must be positive. Furthermore, using the Rayleigh–Ritz theorem [5], it can then be shown that

$$0 < \frac{\boldsymbol{\rho}_{ij}^T \mathbf{P}_{\text{pos}}^- \boldsymbol{\rho}_{ij}}{\rho_{ij}^2} \le \|\mathbf{P}_{\text{pos}}^-\| \qquad (45)$$

for all $\boldsymbol{\rho}_{ij}$.

Using these results, the relationship between the position covariance, residuals, and residual covariances have been examined for each of the four cases using the EKF ($\mathbf{b}_h = \mathbf{0}$ and $\mathbf{B}_h = \mathbf{0}$). As might be expected when relative range measurements are fused, the 2-norm of the relative position covariance $\|\mathbf{P}_{r_i r_j}^{\text{rel}}\|$ reduces much more quickly than without the use of relative measurements. Consequently, as Eq. (45) implies, for $k > m_{\text{in}}$ and a constant R_{kk}, the residual covariance W_{kk}^{EKF} must also reduce rapidly. However, for case 3.1, despite this rapid decrease in the relative range residual covariance, the magnitude of the EKF residual $|\epsilon_k^{\text{EKF}}|$ remains relatively large. This inconsistency between the residual and residual covariance leads to an inaccurate state error covariance, which in turn results in filter divergence. Thus, in this case, it is desirable to increase the residual covariance such that its convergence rate is consistent with that of the residual.

B.   First-Order Robustness Enhancement Algorithms

It has been noted that, when considering a highly observable system, the scalar update appears to be more stable than the matrix update when fusing relative measurements, so long as all the inertial measurements are processed first [8]. The scalar (or "row-by-row") update is so named because it processes the scalar components of the measurement vector one (row) at a time. This is accomplished by considering the simultaneous measurement components to occur consecutively over an infinitesimal span of time. Modifying the EKF matrix update equations in this way results in Algorithm 1, where $\mathbf{H}_k$ refers to the kth row of the $m \times n$ matrix $\mathbf{H}$, ϵ_k refers to the kth component of the $m \times 1$ residual vector $\boldsymbol{\epsilon}$, and R_{kk} refers to the kth diagonal element of the $m \times m$ matrix $\mathbf{R}$. (Alternatively, Crassidis and Junkins [9] offer a variation of this algorithm for the Kalman filter that updates the state error covariance in this sequential manner but only updates the state estimate after all the measurements have been processed.)

This method inherently causes the order in which measurements are processed to become significant. In particular, because the state estimate is updated as each scalar measurement is processed, each subsequent linearization of the measurement model is about a more accurate state estimate, which in turn results in a reduced state error covariance. Consequently, if, in the initial update, processing the inertial measurements can first successfully reduce the state error covariance from a severe level to a moderate level, then the potential for fusion complications is eliminated before the relative measurements are even processed. However, although this would result in filter convergence, this scheme is at best circumstantial and at worst only feasible in the rare instance in which the relative measurements are never processed in the presence of a severe level of state error covariance. In other words, in a less observable system, the initial

processing of the inertial measurements may not result in a significant reduction in the state error covariance. Although the scalar update scheme works for the case 3.1 mission, which uses three inertial measurements, for a single inertial measurement mission, this scheme was shown to be inadequate to prevent filter divergence [7]. The scalar update scheme has similarly been exploited in some radar tracking algorithms where the azimuth measurements, which have insignificant nonlinearities in practical tracking environments, are processed before the range measurements [10]. However, once again, this scheme yields degraded performance when the nonlinearities become more significant.

The next two schemes presented are extensions of the standard filter tuning procedure in which the filter noise is "tuned" to the appropriate value. One tuning parameter of this procedure is the process noise. Because this simulation uses the same dynamic model for the environment and the filter, in general, process noise is not required. Nevertheless, it is not uncommon in practice to add artificial "pseudonoise" to prevent filter divergence due to numerical inadequacies. Employing this strategy, case 3.1 was reexamined with the inclusion of process noise (i.e., $\mathbf{Q}_{\text{spec}} \ne \mathbf{0}$). After evaluating several different levels of process noise in the simulation, it was determined that, to prevent filter divergence, the process noise would need to be so extreme that the filter performance was worse than simply not processing the relative measurements (i.e., case 3.0 without process noise). Although this scheme prevents filter divergence, because the overall goal is to fuse the relative measurements to obtain a more accurate state estimate, using this scheme is ultimately counterproductive.

Another parameter of the filter tuning procedure is the adjustment of the measurement noise. In practice, the true noise associated with a particular measurement is not necessarily accurately known. However, in general, the larger the measurement noise covariance, the less confidence the filter has in the measurement. In this way, measurements can slowly be brought "online" by intentionally giving the filter an initially exaggerated measurement noise covariance and then gradually reducing it until a more realistic value is reached. For example, this could be done for the relative measurements in case 3.1 by initially setting $R_{kk}(t_1) = \tilde{\sigma}_\rho^2$, where $k > m_{\text{in}}$ and $\tilde{\sigma}_\rho \gg \sigma_\rho$, and then reducing $\tilde{\sigma}_\rho$ until it is comparable to σ_ρ. This reduction in measurement noise covariance can be achieved by some chosen functional reduction method [e.g., $R_{kk} = R_{kk}(t)$] or by using an adaptive measurement noise algorithm. Also note that, as seen in Eq. (44), increasing the measurement noise covariance R_{kk} has the desired effect of increasing the residual covariance W_{kk}. Several different systematically reduced and adaptive measurement noise schemes have been evaluated for this purpose. In particular [for $\tilde{\sigma}_\rho^2(t_0) = 50 \text{ km}^2$], the functional method used an exponential function of time to reduce the relative measurement noise covariance, whereas the adaptive algorithm was based on a combination of the algorithm presented in Maybeck [3] and the running-average filter presented in Busse et al. [11].

The running-average (or fading memory) filter described in Algorithm 2 is used to incorporate the measurement noise covariance update R_{kk}^* into the previous measurement noise covariance. In Algorithm 2, m_{in} is the number of inertial measurements ($m_{\text{in}} = 3p$),

---

Algorithm 1   Scalar update algorithm

Given: $\hat{\mathbf{x}}^-$, $\mathbf{P}^-$, $\mathbf{z}$, and $\mathbf{R}$ at time t_d
FOR $k = 1, \dots, m$
    $\epsilon_k = z_k - h_k(\hat{\mathbf{x}}^-)$ and $\mathbf{H}_k = \mathbf{H}_k(\hat{\mathbf{x}}^-)$
    $\mathbf{K} = \mathbf{P}^- \mathbf{H}_k^T / (\mathbf{H}_k \mathbf{P}^- \mathbf{H}_k^T + R_{kk})$
    $\hat{\mathbf{x}}^+ = \hat{\mathbf{x}}^- + \mathbf{K}\epsilon_k$
    $\mathbf{P}^+ = (\mathbf{I} - \mathbf{K}\mathbf{H}_k)\mathbf{P}^-(\mathbf{I} - \mathbf{K}\mathbf{H}_k)^T + R_{kk}\mathbf{K}\mathbf{K}^T$
    $\hat{\mathbf{x}}^- = \hat{\mathbf{x}}^+$ and $\mathbf{P}^- = \mathbf{P}^+$
END FOR (k)
Set: $\hat{\mathbf{x}}^+ = \hat{\mathbf{x}}^-$ and $\mathbf{P}^+ = \mathbf{P}^-$

Algorithm 2   Adaptive measurement noise algorithm

Given $\mathbf{R}^*$ at times t_d and t_{d-w} using Eq. (46)
FOR $k = m_{\text{in}} + 1, \dots, m$
    IF $d \le w$
        $R_{kk}(t_d) = R_{kk}(t_{d-1}) + \frac{R_{kk}^*(t_d) - R_{kk}(t_{d-1})}{d}$
    ELSE
        $R_{kk}(t_d) = R_{kk}(t_{d-1}) + \frac{R_{kk}^*(t_d) - R_{kk}(t_{d-w})}{w}$
    END IF
    IF $R_{kk}(td) < \sigma_\rho^2$
        $R_{kk}(td) = \sigma_\rho^2$
    END IF
END FOR (k)

w is the length of the memory window of the past measurements to be averaged ($w = 20$), and the last IF statement is to prevent the measurement noise covariance from dropping below the variance of the actual measurement noise. The full matrix equation for the update $\mathbf{R}^*$ at discrete measurement time t_d can be written as

$$\mathbf{R}^* = \boldsymbol{\epsilon}\boldsymbol{\epsilon}^T + \mathbf{H}\mathbf{P}^+\mathbf{H}^T \qquad (46)$$

where $\boldsymbol{\epsilon}$, $\mathbf{H}$, and $\mathbf{P}^+$ have been obtained using the a posteriori values at the time of the previous measurement [i.e., $\boldsymbol{\epsilon} = \mathbf{z}(t_{d-1}) - \mathbf{h}(\hat{\mathbf{x}}(t_{d-1}^+))$, $\mathbf{H} = \mathbf{H}(\hat{\mathbf{x}}(t_{d-1}^+))$, and $\mathbf{P}^+ = \mathbf{P}(t_{d-1}^+)$]. Both of these methods demonstrated not only the capacity to prevent filter divergence in case 3.1, but also the ability to decrease the navigation error by correctly incorporating the relative measurements. A summary of the performance of the adaptive method, which performed better and required far less tuning, is available in Table 5 (I-C). Both of these methods achieve this performance by tuning the relative measurement noise such that the filter essentially ignores the relative measurements until the state error covariance is reduced to a moderate level. Consequently, if similarly tuned, these schemes offer similar performance to the selective measurement scheme.

The selective measurement scheme, which has also been used in practice, takes a more direct approach by not introducing the relative measurements until after the state error covariance has converged to an acceptable level (e.g., a moderate level). For example, this can be accomplished by not processing relative range measurements unless the square root of the maximum diagonal elements of $\mathbf{P}_{rr}$ and $\mathbf{P}_{vv}$ are less than the moderate values of σ_r and σ_v, respectively, presented in Table 3. Such a scheme is similar to implementing the scalar update scheme with a residual check that instead ignores measurements only when they violate the residual covariance inconsistency. For example, if $\epsilon_k^2/W_{kk} > \text{tol}$, where tol is some predetermined tolerance, the kth measurement z_k would be ignored by setting $\mathbf{K} = \mathbf{0}$ at the appropriate step in Algorithm 1. However, unlike the selective measurement scheme that has demonstrated effective performance for case 3.1, the residual check in its current form has not proven to be a viable solution for this particular application. The performance of the selective measurement scheme is summarized in Table 5 (I-D).

Although the selective measurement scheme and the adaptive measurement noise scheme have been proven successful, they share two unfortunate traits. First, they require the tuning of an initial parameter or tolerance. In general, filter tuning is problem specific and at times extremely tedious. This can be especially true in this situation where there is a constant tradeoff between robustness and bringing the relative measurements online in a timely manner. Also, even if the tuning turns out to be fairly straightforward, these schemes still do not guarantee suitable robustness outside of that particular tuning regime. Furthermore, to optimize efficiency, the selective measurement scheme would require a comprehensive analysis to determine the ideal state error covariance tolerance and a robust automated implementation method. Finally, the second trait shared by these schemes is that, although they avoid the effects of the fusion complications, they do not yield any additional insight into the cause of these complications. For this reason, the second-order terms normally truncated during the first-order Taylor series expansion have been thoroughly examined.

C. Second-Order Robustness Enhancement Algorithms

The focus of investigating second-order methods is to determine what significance the second-order terms resulting from quadratic nonlinearities that are normally truncated have in regards to the

experienced fusion complications. Maybeck [3] states that "...empirical results have corroborated that nonlinear effects are most important when noise inputs are small while estimation error variance is relatively large." This is exactly the scenario presented in case 3.1 when no robustness enhancement schemes are implemented. The first-order noise schemes exploit this fact by using noise to account for model inadequacies due to neglecting higher-order terms. To verify this, case 3.1 was reexamined with the implementation of the GSF in place of using the EKF with artificial or exaggerated noise. The resulting performance is summarized in Table 5 (scheme II). Notice that, although the GSF outperforms the first-order methods, the results are quite comparable. This indicates that the measurement noise scheme is doing an adequate job of accounting for the second-order terms that the EKF neglects. The selective measurement scheme, on the other hand, accomplishes this by not introducing the relative measurements until the second-order terms have become negligible. Finally, although in this case the slight increase in accuracy achieved by the GSF does come at a cost of roughly a 50% increase in computation time, it does have the added benefit of general robustness without any required filter tuning. Furthermore, as will be shown later, if the second-order state estimate propagation term is not required (i.e., $\mathbf{b}_f = \mathbf{0}$), there is only about a 20% increase in computation time.

The challenge is to determine why the second-order terms are so much more significant when the relative measurements are fused. To accomplish this, Eqs. (6) and (40) are used to reduce Eq. (22) to

$$b_{f_i} = \tfrac{1}{2}\text{trace}(\boldsymbol{\Delta}_{f_i}\mathbf{P}_{rr}) = \begin{cases} 0 & 1 \le i \le n/2 \\ \tfrac{1}{2}\text{trace}(\mathbf{G}'_{jk}\mathbf{P}_{r_jr_j}) & n/2 < i \le n \end{cases} \qquad (47)$$

where the subscript j refers to the spacecraft number ($j = 1, \ldots, p$), the subscript k refers to the x, y, or z component of $\mathbf{v}_j$ or $\mathbf{g}_j$ ($k = 1, 2, 3$, respectively) corresponding to f_i, and $\mathbf{G}'_{jk}$ is defined in Eq. (7). Likewise, using Eqs. (12) and (40), Eqs. (27) and (31) can be reduced to

$$b_{h_k} = \tfrac{1}{2}\text{trace}(\boldsymbol{\Delta}_{h_k}\mathbf{P}_{rr}^-) = \tfrac{1}{2}\text{trace}(\boldsymbol{\Theta}'_{ij}\mathbf{P}_{\text{pos}}^-) \qquad (48)$$

and

$$B_{h_{kk}} = \tfrac{1}{2}\text{trace}(\boldsymbol{\Delta}_{h_k}\mathbf{P}_{rr}^-\boldsymbol{\Delta}_{h_k}\mathbf{P}_{rr}^-) = \tfrac{1}{2}\text{trace}(\boldsymbol{\Theta}'_{ij}\mathbf{P}_{\text{pos}}^-\boldsymbol{\Theta}'_{ij}\mathbf{P}_{\text{pos}}^-) \qquad (49)$$

where the subscript j refers to the primary spacecraft number, and the subscript i refers to the station number (for inertial measurements) or the secondary spacecraft number (for relative measurements) that is tracking the primary; and $\boldsymbol{\Theta}'_{ij}$ and $\mathbf{P}_{\text{pos}}^-$ are defined in Eqs. (13) and (43), respectively.

The following theorem adapted from Horn and Johnson [5] will be useful: *Theorem 1:* For any two symmetric positive semidefinite matrices $\mathbf{A}$ and $\mathbf{B}$, the matrix $\mathbf{A}\mathbf{B}$ has real nonnegative eigenvalues. Consequently,

$$\text{trace}(\mathbf{A}\mathbf{B}) = \sum_i \lambda_i(\mathbf{A}\mathbf{B}) \ge 0 \quad \text{and}$$

$$0 \le \text{trace}(\mathbf{A}\mathbf{B}\mathbf{A}\mathbf{B}) \le [\text{trace}(\mathbf{A}\mathbf{B})]^2$$

Anticipating that Theorem 1 will require a symmetric positive semidefinite matrix, it is also useful to define the matrix $(\|\mathbf{A}\|\mathbf{I} - \mathbf{A})$, which for any symmetric $\mathbf{A}$ is symmetric positive semidefinite by Theorem 2, where, in general, $\|\cdot\|$ indicates the vector or matrix 2-norm and $\lambda_i(\cdot)$ indicates the ith component of the corresponding

Table 5 Robustness enhancement scheme performance comparison

Scheme	$\bar{P}_{xx}^{1/2}(t_f)$, m	$\bar{P}_{yy}^{1/2}(t_f)$, m	$\bar{P}_{zz}^{1/2}(t_f)$, m	$\bar{P}_{\dot{x}\dot{x}}^{1/2}(t_f)$, mm/s	$\bar{P}_{\dot{y}\dot{y}}^{1/2}(t_f)$, mm/s	$\bar{P}_{\dot{z}\dot{z}}^{1/2}(t_f)$, mm/s
0	0.532	1.164	1.463	0.473	1.230	0.980
I-C	0.390	0.843	0.702	0.372	0.568	0.709
I-D	0.393	0.871	0.736	0.393	0.600	0.744
II	0.365	0.804	0.682	0.353	0.555	0.672

vector of eigenvalues $\boldsymbol{\lambda}(\cdot)$.*Theorem 2:* For any symmetric matrix $\mathbf{A}$, the matrix $(\|\mathbf{A}\|\mathbf{I} - \mathbf{A})$ is symmetric positive semidefinite.

Proof.

$$\lambda_i(\|\mathbf{A}\|\mathbf{I} - \mathbf{A}) = \|\mathbf{A}\| - \lambda_i(\mathbf{A}) = \max|\lambda(\mathbf{A})| - \lambda_i(\mathbf{A}) \geq 0$$

Finally, combining Theorems 1 and 2, the following theorem, adapted from Ran and Reurings [12], is obtained.*Theorem 3:* For any symmetric matrix $\mathbf{A}$ and symmetric positive semidefinite matrix $\mathbf{B}$,

$$\text{trace}(\mathbf{AB}) \leq \|\mathbf{A}\|\text{trace}(\mathbf{B})$$

Proof:

$$\text{trace}((\|\mathbf{A}\|\mathbf{I} - \mathbf{A})\mathbf{B}) \geq 0 \quad (\text{Thms.1 and 2})$$

$$\text{trace}(\|\mathbf{A}\|\mathbf{B} - \mathbf{AB}) \geq 0 \qquad \|\mathbf{A}\|\text{trace}(\mathbf{B}) - \text{trace}(\mathbf{AB}) \geq 0$$

$$\|\mathbf{A}\|\text{trace}(\mathbf{B}) \geq \text{trace}(\mathbf{AB})$$

Recognizing that $\mathbf{G}'_{jk}$ is symmetric and $\mathbf{P}_{r_j r_j}$ is symmetric positive definite, applying Theorem 3 to Eq. (47) results in the following bound on b_{f_i} for all $i > n/2$:

$$|b_{f_i}| \leq \tfrac{1}{2}\|\mathbf{G}'_{jk}\|\text{trace}(\mathbf{P}_{r_j r_j}) \tag{50}$$

Likewise, since $\boldsymbol{\Theta}'_{ij}$ is symmetric and positive semidefinite by Eq. (54) and $\mathbf{P}^-_{\text{pos}}$ is symmetric positive definite, Theorems 1 and 3 can be applied to Eq. (48) to obtain bounds for b_{h_k} yielding

$$0 \leq b_{h_k} \leq \tfrac{1}{2}\|\boldsymbol{\Theta}'_{ij}\|\text{trace}(\mathbf{P}^-_{\text{pos}}) \tag{51}$$

and applied to Eq. (49) to obtain bounds for $B_{h_{kk}}$, as

$$0 \leq B_{h_{kk}} \leq \tfrac{1}{2}(\|\boldsymbol{\Theta}'_{ij}\|\text{trace}(\mathbf{P}^-_{\text{pos}}))^2 \tag{52}$$

Notice that since $B_{h_{kk}} \geq 0$, it has the desired effect of increasing the relative range residual covariance W_{kk} [see Eq. (30)]. Next, since $\mathbf{G}'_{jk}$ and $\boldsymbol{\Theta}'_{ij}$ are symmetric, their 2-norm is the maximum of the absolute value of their eigenvalues. Thus, computing the eigenvalues of $\mathbf{G}'_{jk}$ and $\boldsymbol{\Theta}'_{ij}$ results in

$$\boldsymbol{\lambda}(\mathbf{G}'_{jk}) = \frac{3\mu}{2\|\mathbf{r}_j\|^5}\begin{bmatrix} 2r_{j_k} \\ -r_{j_k} + \sqrt{5r_{j_k}^2 + 4\|\mathbf{r}_j\|^2} \\ -r_{j_k} - \sqrt{5r_{j_k}^2 + 4\|\mathbf{r}_j\|^2} \end{bmatrix}, \qquad \|\mathbf{G}'_{jk}\| \leq \frac{6\mu}{\|\mathbf{r}_j\|^4} \tag{53}$$

and

$$\boldsymbol{\lambda}(\boldsymbol{\Theta}'_{ij}) = \frac{1}{\rho_{ij}}\begin{bmatrix} 1 \\ 1 \\ 0 \end{bmatrix}, \qquad \|\boldsymbol{\Theta}'_{ij}\| = \frac{1}{\rho_{ij}} \tag{54}$$

Notice that, although an equality for $\|\mathbf{G}'_{jk}\|$ cannot be determined in general, the term can still be conservatively bounded. These results indicate that the bounds on the second-order terms are functions solely of the trace of the appropriate state error covariance matrix and the orbit radius magnitude $\|\mathbf{r}_j\|$ or the range measurement magnitude ρ_{ij}.

To verify the bound on b_{f_i}, Eq. (47) was evaluated for various random values of $\mathbf{P}_{r_j r_j}$ and $\mathbf{r}_j$, for a set $\|\mathbf{r}_j\| = R_M$, the radius of the moon. This particular constraint value was chosen because it allows for the maximum value obtainable by b_{f_i}. According to Eq. (53), the upper bound on $\|\mathbf{G}'_{jk}\|$ is maximized by minimizing $\|\mathbf{r}_j\|$. Consequently, since for any lunar orbit $\|\mathbf{r}_j\| > R_M$, in a real application $\|\mathbf{G}'_{jk}\|$, and thus b_{f_i}, will never achieve values higher then those computed with $\|\mathbf{r}_j\| > R_M$. Thus, as illustrated by the solid lines in Fig. 11, b_{f_i} is in fact conservatively bounded by Eq. (50).

Similarly, to verify the bounds on b_{h_k} and $B_{h_{kk}}$, Eqs. (48) and (49) were evaluated for various random values of $\mathbf{P}^-_{\text{pos}}$ and $\boldsymbol{\rho}_{ij}$ for a set $\|\boldsymbol{\rho}_{ij}\| = \rho_{ij}$. This time, the random values of $\boldsymbol{\rho}_{ij}$ were constrained
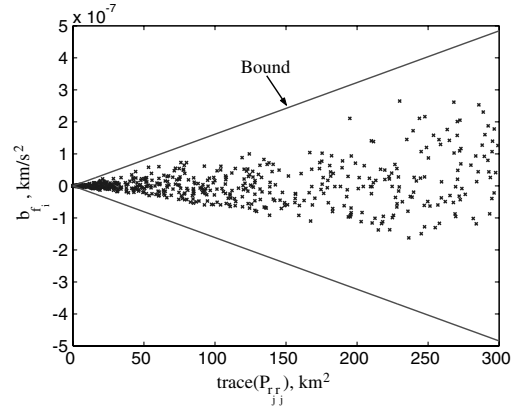

Fig. 11 Evaluation of second-order term b_{f_i} for $\|\mathbf{r}_j\| > R_M$ and random $\mathbf{P}_{r_j r_j}$ with the corresponding bounds of Eq. (50).

using multiple values of ρ_{ij} to illustrate the sensitivity of b_{h_k} and $B_{h_{kk}}$ to the range measurement magnitude. In particular, it was desirable to compare inertial range measurement magnitudes with relative range measurement magnitudes. In general, as seen in Eq. (54), $\|\boldsymbol{\Theta}'_{ij}\|$ is maximized by minimizing ρ_{ij}. Thus, to demonstrate the maximum values obtainable for b_{h_k} and $B_{h_{kk}}$ given an inertial range measurement, it is necessary to consider a constraint value that is on order with the smallest possible inertial range measurement. Although, as mentioned earlier, the smallest inertial range measurements considered in this scenario are on the order of 0.645×10^5 km (for L_2), suppose instead a lunar surface beacon was available such that the smallest inertial range measurement was on the order of hundreds of kilometers. Because of this consideration, a constraint value of $\rho_{ij} = 500$ km was chosen for the inertial range measurement magnitude.

Relative range measurements, on the other hand, are not necessarily limited in magnitude. Depending on the mission, formation baselines between spacecraft can range from the order of hundreds of meters to hundreds of kilometers. Consequently, a constraint value equivalent to the most common relative range magnitude (between coplanar spacecraft) was chosen to be $\rho_{ij} = 10$ km. Using these values, the solid lines in Fig. 12 illustrate that b_{h_k} and $B_{h_{kk}}$ are in fact bounded by Eqs. (51) and (52). Notice that, even for the smallest possible inertial range measurement, the second-order terms for the relative range measurement are 2 orders of magnitude larger. Finally, as implied later, the trace values in Fig. 12b are intentionally twice that of Fig. 12a due to the corresponding definition of $\mathbf{P}^-_{\text{pos}}$ in Eq. (43).

Although Figs. 11 and 12 demonstrate the range of possible values for the second-order terms, these values must be put into context to determine their significance. Thus, recalling Eq. (21), it is necessary to examine the order of b_{f_i} relative to f_i. First, as is true in this case, suppose that initially $\mathbf{P}_{r_i r_i} \approx \mathbf{P}_{r_j r_j} \approx \sigma_r^2 \mathbf{I}$ and $\mathbf{P}_{r_i r_j} \approx \mathbf{P}_{r_j r_i} \approx \mathbf{0}$. Using these assumptions, the "worst case" order of $|f_i|$ and $|b_{f_i}|$ can be approximated as

$$|f_i| = |g_{j_k}| = \frac{\mu}{\|\mathbf{r}_j\|^3}|r_{j_k}| \sim \frac{\mu}{\|\mathbf{r}_j\|^2}$$

$$|b_{f_i}| \leq \frac{3\mu}{\|\mathbf{r}_j\|^4}\text{trace}(\mathbf{P}_{r_j r_j}) \sim \frac{9\mu\sigma_r^2}{\|\mathbf{r}_j\|^4} \tag{55}$$

which, for $\|\mathbf{r}_j\| > R_M$, $|f_i|$ agrees with $g_M = 1.6$ m/s^2 and $|b_{f_i}|$ agrees with the bounds in Fig. 11. Furthermore, since $\|\mathbf{r}_j\| > R_M$, even for a severe level of covariance ($\sigma_r \sim 10$ km), $|b_{f_i}|$ will typically be at least 4 orders of magnitude smaller than $|f_i|$ and consequently negligible. This fact has been further demonstrated by successfully implementing the GSF in case 3.1 without the second-order state estimate propagation term (i.e., $\mathbf{b}_f = \mathbf{0}$). This implies that the same GSF could easily be applied to higher fidelity gravity models. These results similarly apply to Earth orbiting missions [7].
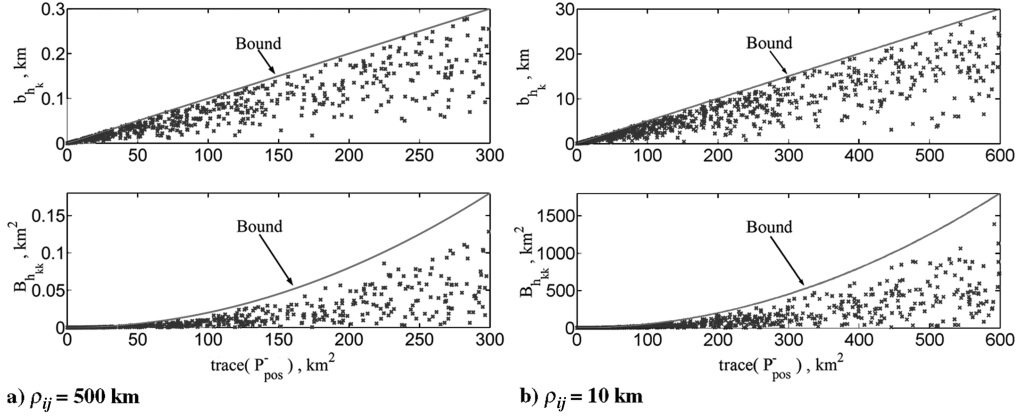
a) $\rho_{ij} = 500$ km   **b)** $\rho_{ij} = 10$ km

Fig. 12   Evaluation of second-order terms b_{h_k} and $B_{h_{kk}}$ for random $\mathbf{P}_{\mathrm{pos}}^-$ with the corresponding upper bounds of Eqs. (51) and (52).

Likewise, recalling Eqs. (26) and (30), it is necessary to examine the order of b_{h_k} relative to $|\epsilon_k^{\mathrm{EKF}}|$ and $B_{h_{kk}}$ relative to W_{kk}^{EKF} [see Eq. (44)]. Based on the previous covariance assumptions, $\mathbf{P}_{\mathrm{pos}}^- = \mathbf{P}_{r_j r_j}^- \approx \sigma_r^2 \mathbf{I}$ for inertial measurements ($1 \le k \le m_{\mathrm{in}}$) and $\mathbf{P}_{\mathrm{pos}}^- = \mathbf{P}_{r_i r_j}^{\mathrm{rel}} \approx 2\sigma_r^2 \mathbf{I}$ for relative measurements ($k > m_{\mathrm{in}}$). Using these assumptions, the worst case order of $|\epsilon_k^{\mathrm{EKF}}|$ and b_{h_k} can be approximated as

$$|\epsilon_k^{\mathrm{EKF}}| \sim \sqrt{W_{kk}^{\mathrm{EKF}}} \sim \begin{cases} \sigma_{\mathbf{r}} & 1 \le k \le m_{\mathrm{in}} \\ \sqrt{2}\sigma_r & k > m_{\mathrm{in}} \end{cases}$$

$$b_{h_k} \le \frac{1}{2\rho_{ij}}\mathrm{trace}(\mathbf{P}_{\mathrm{pos}}^-) \sim \begin{cases} 3\sigma_r^2/(2\rho_{ij}) & 1 \le k \le m_{\mathrm{in}} \\ 3\sigma_r^2/\rho_{ij} & k > m_{\mathrm{in}} \end{cases} \tag{56}$$

whereas the worst case order of W_{kk}^{EKF} (for $R_{kk} = \sigma_\rho^2 \ll \sigma_r^2$) and $B_{h_{kk}}$ are approximated as

$$W_{kk}^{\mathrm{EKF}} \sim \begin{cases} \sigma_r^2 & 1 \le k \le m_{\mathrm{in}} \\ 2\sigma_r^2 & k > m_{\mathrm{in}} \end{cases}$$

$$B_{h_{kk}} \le \frac{1}{2}\left(\frac{1}{\rho_{ij}}\mathrm{trace}(\mathbf{P}_{\mathrm{pos}}^-)\right)^2 \sim \begin{cases} 9\sigma_r^4/(2\rho_{ij}^2) & 1 \le k \le m_{\mathrm{in}} \\ 18\sigma_r^4/\rho_{ij}^2 & k > m_{\mathrm{in}} \end{cases} \tag{57}$$

all of which agree with the appropriate bounds in Fig. 12.

As alluded to earlier, the significance of the second-order terms is now directly related to the magnitude of the range measurement, regardless of if it is an inertial or relative measurement. In fact, in situations where the formation can be grossly distorted such that the baselines between spacecraft are similar in size to the inertial measurements, the EKF will converge for a severe level of covariance without the implementation of any robustness enhancement schemes [7]. Similarly, even if it is supposed that, for inertial range measurements ρ_{ij} is on the order of thousands of kilometers (instead of the actual order of 10^5 km), even for a severe level of covariance, b_{h_k} would typically be at least 3 orders of magnitude smaller than $|\epsilon_k^{\mathrm{EKF}}|$ and $B_{h_{kk}}$ would typically be at least 5 orders of magnitude smaller than W_{kk}^{EKF}; consequently, both are negligible. Conversely, because for relative range measurements ρ_{ij} is on the order of tens of kilometers, for a severe level of covariance, b_{h_k} and $B_{h_{kk}}$ will typically be of about the same order of magnitude or larger than $|\epsilon_k^{\mathrm{EKF}}|$ and W_{kk}^{EKF}, respectively, and consequently quite significant.

Thus, the GSF has demonstrated the ability to prevent divergence even if the second-order terms are added only to the relative measurement components in the update equations. However, although doing so can decrease computation costs, this must be done cautiously so as to avoid neglecting any significant off-diagonal terms $B_{h_{jk}}$ that are correlated with the relative measurements.

Conversely, even if it is not practical to implement the GSF, the bounds developed in Eqs. (51) and (52) can still be used to quantify the overall significance of the quadratic nonlinearities by determining at what covariance level the second-order terms become insignificant enough to allow the introductions of small magnitude range measurements. Although the covariance levels denoted "moderate" and "severe" are defined for this case in Table 3, in general, these two concepts are intended to indicate soft measures of covariance levels such that fusing relative measurements result in filter convergence for the former and filter divergence for the latter. The exact region that defines these levels is problem dependent, or more precisely, a function of the magnitude of the range measurement. For example, if instead $\rho_{ij} = 0.1$ km is considered, the covariance level definitions in Table 3 no longer apply. Moreover, second-order terms would no longer be adequate to prevent filter divergence for case 3.1, as this combination of covariance and range magnitude will likely cause cubic nonlinearities to become significant.

Consequently, instead consider the more aptly defined "critical" covariance, which is defined as the covariance at which point $b_{h_k} \approx |\epsilon_k^{\mathrm{EKF}}|$.[††] Thus, for covariance levels near or larger than the critical covariance, the quadratic nonlinearities are significant. Equating b_{h_k} and $|\epsilon_k^{\mathrm{EKF}}|$ for the relative measurement case[‡‡] ($k > m_{\mathrm{in}}$) of Eq. (56) and solving for the σ_r, the critical covariance can then be defined as the square of

$$\sigma_r^{\mathrm{crit}} = \frac{\sqrt{2}}{3}\rho_{ij} \tag{58}$$

Therefore, in case 3.1 when $\rho_{ij} = 10$ km, the critical value of σ_r is 4.7 km, which, as would be expected, is roughly midway between the moderate and severe levels defined in Table 3. Also, this critical covariance results in a trace$(\mathbf{P}_{\mathrm{pos}}^-) \approx 133$ km^2, which, as seen in Fig. 12, corresponds to a maximum value for b_{h_k} that is equal to the expected value for the residual, $|\epsilon_k^{\mathrm{EKF}}| \approx 6.7$ km, at that particular covariance level.

To further illustrate this concept, the two-spacecraft formation of case 1.1 was reexamined for various combinations of position covariance levels σ_r^2 (with $\sigma_v \sim 10^{-4}\sigma_r$) and relative range magnitudes ρ_{12} (obtained by altering the formation spacing). In Fig. 13, the filled circles denote instances in which the filter converged, whereas the "×" markers denote instances in which the filter diverged. As expected, instances in which the covariance is comparable to the critical value are subject to potential fusion complications. Thus, this analysis results in the rule of thumb that range measurements of magnitude ρ_{ij} must be processed with extreme caution when in the presence of position covariance levels on the order of σ_r^{crit}.

[††]The $b_{h_k} \approx |\epsilon_k^{\mathrm{EKF}}|$ definition was chosen instead of $B_{h_{kk}} \approx W_{kk}^{\mathrm{EKF}}$ because, as implied in the discussion following Eq. (57), as well as in Maybeck [3], the b_{h_k} terms are typically much more significant. However, using this alternate definition, the resulting critical value would be $\sqrt{2}$ times smaller than that of Eq. (58).

[‡‡]The relative measurement case was used because not only is it more likely to cause filter complications, but also because it results in a more conservative value: using the inertial measurement case ($1 \le k \le m_{\mathrm{in}}$), the resulting critical value would be $\sqrt{2}$ times larger than that of Eq. (58).
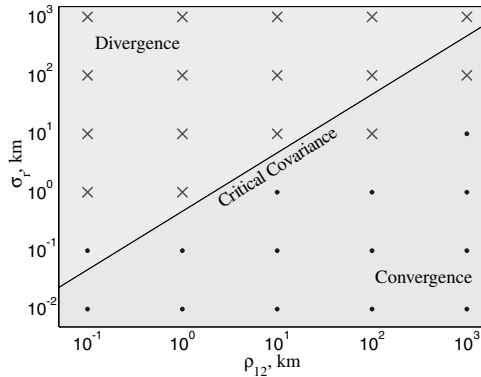
Fig. 13 Navigation performance for various instances of case 1.1 with the corresponding critical covariance defined by σ_r^{crit}.

D. Robustness Enhancement Simulation Results

Several schemes have been examined to increase filter robustness when fusing inertial and relative range measurements. Table 5 summarizes the performance of the following schemes at a final time of t_f equal to the orbital period: 0) no scheme for case 3.0, I-C) adaptive measurement noise scheme for case 3.1, I-D) selective measurement scheme for case 3.1, and II) second-order method for case 3.1.

The overbar on the state error covariance P indicates that the values shown are the average values of all four spacecraft. This was done because the state error covariance history of each spacecraft is nearly identical. By successfully fusing the relative measurements using one of the aforementioned robustness enhancements schemes, the filter achieves essentially the same increase in navigation as described in Table 2 for case 2. Thus, the navigation state error plots for case 3.1, scheme I or II, have not been presented here as they look very similar to what was seen in Fig. 10. This result is to be expected though, because after the covariance level is quickly reduced, case 3 is essentially the same as case 2. One difference, however, can be found in the rate of convergence. Recall that, for the Z_I position covariance to converge to less than the measurement noise of 5 m, case 2.1 required only 28 measurement updates. Now, for case 3.1, schemes I-C and II required 51 measurement updates and scheme I-D required 58 measurement updates (recall updates occur every minute). This decrease in convergence rate is because, not only is the initial covariance larger but, more importantly, the relative measurements are not fully used during the first several updates.

VI.   Conclusions

One contribution of this research is the development of the relationship between observer-formation geometry and navigation performance. It has been demonstrated that certain geometries can lead to a reduction in observability and consequently a decrease in navigation accuracy. Using the LTI observability condition, the following observability-reducing geometries were determined:

1) One spacecraft and the two or more stations tracking it are collinear.

2) One spacecraft and the three or more stations tracking it are coplanar.

3) Two spacecraft and the station(s) tracking each are collinear.

4) The line connecting two spacecraft is parallel to the line connecting the two stations tracking each spacecraft.

5) Three spacecraft are collinear.

The decrease in the robustness of the EKF resulting from fusing inertial and relative range measurements was then considered. In particular, after reviewing some common first-order methods, second-order terms that are normally truncated were thoroughly examined and the exact cause of the inertial-relative measurement fusion complications was determined. It was found that, although these terms are negligible for large inertial range measurements, they can become quite significant when using small relative range measurements. This is especially true considering that the smaller relative range measurements will typically be more accurate. More specifically, however, it turns out that the magnitude of the range measurement poses the potential problem, not the measurement type, be it inertial or relative. Thus, any relatively small magnitude range measurement must be processed with extreme caution when in the presence of state error covariances on the order of the critical covariance, $\sigma_r^{\text{crit}} = (\sqrt{2}/3)\rho_{ij}$.

References

[1] Huxel, P. J., "Navigation Algorithms and Observability Analysis for Formation Flying Missions," Ph.D. Thesis, Univ. of Texas, Austin, TX, May 2006.
[2] Gelb, A., *Applied Optimal Estimation*, MIT Press, Cambridge, MA, 1974, pp. 180–192.
[3] Maybeck, P. S., *Stochastic Models, Estimation, and Control*, Vol. 2, Academic Press, New York, 1982, pp. 122–123, 224–227.
[4] Chen, C.-T., *Linear System Theory and Design*, 3rd ed., Oxford Univ. Press, Oxford, England, U.K., 1999, p. 153.
[5] Horn, R. A., and Johnson, C. R., *Matrix Analysis*, Cambridge Univ. Press, Cambridge, MA, 1985, pp. 176, 465.
[6] Lay, D. C., *Linear Algebra and Its Applications*, 3rd ed., Addison Wesley, Reading, MA, 2003, pp. 68, 258–259.
[7] Huxel, P. J., and Bishop, R. H., "Fusing Inertial and Relative Measurements for Inertial Navigation in the Presence of Large State Error Covariances," American Astronautical Society Paper 06-126, Jan. 2006.
[8] Huxel, P. J., and Bishop, R. H., "Navigation Algorithms for Formation Flying Missions," *2nd International Symposium on Formation Flying Missions and Technologies*, International Federation of Automatic Control Paper 54, Sept. 2004.
[9] Crassidis, J. L., and Junkins, J. L., *Optimal Estimation of Dynamic Systems*, CRC Press, Boca Raton, FL, 2004, pp. 259–260.
[10] Park, S.-T., and Lee, J. G., "Design of a Practical Tracking Algorithm with Radar Measurements," *IEEE Transactions on Aerospace and Electronic Systems*, Vol. 34, No. 4, Oct. 1998, pp. 1337–1344. doi:10.1109/7.722718
[11] Busse, F. D., How, J. P., and Simpson, J.,"Demonstration of Adaptive Extended Kalman Filter Low-Earth-Orbit Formation Estimation Using CDGPS," *Journal of the Institute of Navigation*, Vol. 50, No. 2, 2003, pp. 79–93, http://www.ion.org/publications/toc/journal4756.htm#50.
[12] Ran, A. C., and Reurings, M. C., "A Fixed Point Theorem in Partially Ordered Sets and Some Applications to Matrix Equations," *Proceedings of the American Mathematical Society*, Vol. 132, American Mathematical Society, Providence, RI, Sept. 2003, pp. 1435–1443.